

# Kinetics of phase separation in two-dimensional systems with competing interactions

Celeste Sagui and Rashmi C. Desai

*Department of Physics, University of Toronto, Toronto, Ontario, Canada M5S 1A7*

(Received 30 September 1993)

The kinetics of supercrystal formation in quenched systems with a scalar order parameter and competing interactions is studied. Systems with nonconserved order parameter (a uniaxial ferromagnetic film) and with conserved order parameter (a binary mixture of amphiphilic molecules at the water-air interface) are considered. The competition between the long-range repulsive interaction of the dipolar type and the short-range attractive interaction due to surface tension leads to the formation of periodically modulated domains. The phase-separation dynamics is simulated using the appropriate Langevin equation. The initial-stage results related to the phase separation and cluster shape transitions are described.

PACS number(s): 05.70.Fh, 61.20.Ja, 61.50.Ks, 64.60.-i

## I. INTRODUCTION

The kinetics of first-order phase transitions has been studied in a wide variety of systems and it is a very topical area in nonequilibrium statistical physics [1]. In this paper we study a broad class of systems in which a rapid quench from a high-temperature homogeneous state to the temperature much below the critical temperature leads to both phase segregation and supercrystal ordering.

The time evolution of phase-separating systems is typically characterized by a single time-dependent length scale, the average domain size  $R(t)$  which often grows as a power law  $R \sim t^m$ . Here  $m$  is the growth exponent and characterizes the mechanism driving the phase separation. Phase-separating systems may be classified into a small number of universality classes, where each member of a given class shares the same kinetic properties. The simplest of these universality classes, viz., model A and model B, correspond to a system with a scalar nonconserved and a scalar conserved order parameter respectively. In model A, the growth is driven by the local curvature and is characterized by  $m = 1/2$  [2]; in model B phase separation takes place by a long-range diffusion and is characterized by  $m = 1/3$  [3].

The systems studied in this paper are modeled by augmenting the models A and B with a competing, nonlocal, long-range repulsive interaction (LRR) in the free-energy functional. Competing interactions in systems whose constituents simultaneously experience mutual magnetostatic or electrostatic repulsion and a short-range attractive interaction lead to the formation of a rich variety of spatially modulated phases, termed supercrystals. For such systems, the free energy contributed by the LRR is reduced by spatial modulations in the corresponding order-parameter field. Domains are regions of uniform amplitude of the order parameter, separated from one another by domain boundaries or walls. The tendency of the LRR for continued subdivision of domains is balanced by the energetic cost of the formation of the interfaces. A new characteristic length scale,

the modulation period, results as a balance between the strength of the LRR and the finite domain-wall energy. Periodic modulations of the magnetization or polarization can be seen in examples such as uniaxial ferromagnetic films [4], ferromagnetic surface layers [5], ferrofluid systems [6], and ferroelectrics [7]. Completely equivalent to these systems, at least at the level of mean-field theory, are two-dimensional binary mixtures of monomolecular amphiphilic films confined to an air-water interface such as Langmuir monolayers [8]. Other interesting examples include cholesteric liquid crystals [9], charge-density waves [10], the primate visual cortex [11], and ceramic compounds with a long-range Coulombic interaction [12].

We have studied the dynamics of quenched quasi-two-dimensional systems with a scalar order parameter and competing interactions. We denote such systems with conserved (nonconserved) order parameter and with a long-range repulsive interaction as model  $B_L$  (model  $A_L$ ) and abbreviate it as  $MB_L$  ( $MA_L$ ). Since some aspects of the early stage results for  $MA_L$  [13] have previously been presented; in this paper we shall concentrate specifically on  $MB_L$  [14].

After the system is quenched, it simultaneously segregates in two phases and creates a supercrystal order corresponding to modulated structures with either lamellar or hexagonal symmetry. Although these processes are simultaneous, the time evolution is characterized by three stages. The early-time regime corresponds to the initial phase segregation and the emergence of polydisperse domains: the instability amplifies the fluctuations present in the initial conditions, saturates them, and forms sharp interfaces. The intermediate-time regime corresponds to the crossover from the maximally unstable wave number that controls the initial fluctuations to the equilibrium wave number: during this stage the domains become monodisperse. The late-time regime corresponds to an ordering process and is mainly driven by defect collisions.

In this paper, we report on the results related to initial stages, i.e., the early and intermediate times. We have presented the results related to the late times for the hexagonal phase elsewhere [15]. This late stage work has

now been extended to both hexagonal and stripe phases and will be described in detail in a future publication [16]. A brief summary of the paper is as follows. In Sec. II we present the mathematical model we will use. In Sec. III we give the phase diagram corresponding to a set of parameters of our simulations. In Sec. IV we present details of the time regimes concentrating on the initial stages and linear analysis. In Sec. V we give the results of the numerical simulation for the quenches into the stripe phase and the hexagonal phase from an initial homogeneous high temperature phase. Section VI is reserved for a brief summary.

## II. MODEL

The free-energy functional  $F$  of our system is the usual Landau-Ginzburg-Wilson free energy modified in such a way as to account for the contribution of the LRRI. It consists of both a local and a nonlocal term. In terms of the order-parameter field  $\phi$ , it is written as

$$F\{\phi\} = F_L\{\phi\} + F_{NL}\{\phi\}, \quad (1)$$

where the local term has an *attractive* square gradient term

$$F_L\{\phi\} = \int d^d r \left[ f(\phi) + \frac{\kappa}{2} (\nabla\phi)^2 \right], \quad (2)$$

and the nonlocal term represents the *repulsive* interactions

$$F_{NL}\{\phi\} = \frac{\alpha}{2} \int d^d r d^d r' \phi(\mathbf{r}') g(|\mathbf{r} - \mathbf{r}'|) \phi(\mathbf{r}). \quad (3)$$

Here  $\kappa$  and  $\alpha$  are positive phenomenological constants, which describe, respectively, the range of the short-range attractive force and the strength of the LRRI. The bulk free energy  $f(\phi)$  is assumed to have a stable single-well structure if the temperature is greater than the critical temperature  $T_c$  and a double-well structure if  $T < T_c$ ,

$$f(\phi) = \frac{-r}{2} \phi^2 + \frac{u}{4} \phi^4 - H\phi, \quad (4)$$

where  $r$  and  $u$  are positive phenomenological constants and  $H$  is an external field that is assumed to couple linearly to the order parameter. The latter will only be relevant for  $MA_L$ .

The time evolution of such a system following a deep quench from a high-temperature disordered phase is given by the appropriate Langevin equations:

$$\frac{\partial\phi(\mathbf{r}, t)}{\partial t} = -M(-\nabla^2)^n \frac{\delta F}{\delta\phi} + \zeta(\mathbf{r}, t), \quad (5)$$

where  $M$  is the mobility (assumed constant) and  $\zeta(\mathbf{r}, t)$  is the Gaussian random noise that results from the coarse-graining procedure. The second moment of the noise is related to the mobility through a fluctuation-dissipation relation

$$\langle \zeta(\mathbf{r}, t) \zeta(\mathbf{r}', t') \rangle = 2k_B T M (-\nabla^2)^n \delta(\mathbf{r} - \mathbf{r}') \delta(t - t'), \quad (6)$$

where  $k_B$  is the Boltzmann constant and  $T$  the temperature of the system. For a system with a conserved (non-conserved) order parameter,  $n = 1$  ( $n = 0$ ).

The order parameter can be written as  $\phi(\mathbf{r}, t) = \overline{\phi(t)} + \Delta\phi(\mathbf{r}, t)$ . At any given time,  $\frac{1}{L^d} \int d^d r \phi(\mathbf{r}, t) = \overline{\phi(t)}$  and  $\int d^d r \Delta\phi(\mathbf{r}, t) = 0$ . Since in  $MB_L$  the concentration is conserved,  $\overline{\phi} = 0$  for a critical quench during the phase separation. If a field is not turned on after quenching in  $MA_L$ , the average magnetization is also zero. In both cases, the resulting morphology is a convoluted stripe-like pattern. By setting  $\overline{\phi} \neq 0$ , one can get circular isolated domains instead of percolating stripes. In  $MB_L$  this can be achieved by making  $\overline{\phi(t)} = \phi_0 = \text{const}$  before quenching;  $\phi_0$  is called the off criticality and the quench is said to be off critical. In  $MA_L$  this can be achieved by turning on an external field  $H$ . In this case  $\overline{\phi}$  varies with time, though eventually it reaches an equilibrium value that depends on the field.

It is convenient to express the above equations in dimensionless form by using the transformations

$$\mathbf{x} = \left( \frac{r}{\kappa} \right)^{\frac{1}{2}} \mathbf{r},$$

$$\tau = 2Mr \left( \frac{r}{\kappa} \right)^n t,$$

$$\psi(\mathbf{x}, \tau) = \left( \frac{u}{r} \right)^{\frac{1}{2}} [\phi(\mathbf{r}, t) - \overline{\phi(t)}], \quad (7)$$

$$\overline{\psi(\tau)} = \left( \frac{u}{r} \right)^{\frac{1}{2}} \overline{\phi(t)}.$$

The equation of motion for the dimensionless concentration or magnetization *fluctuations*  $\psi(\mathbf{x}, \tau)$  in the two-phase region is

$$\begin{aligned} \frac{\partial\psi(\mathbf{x}, \tau)}{\partial\tau} = & \frac{(-\nabla^2)^n}{2} \left[ (\nabla^2 + q_c^2(\tau)) \psi(\mathbf{x}, \tau) - 3\overline{\psi(\tau)} \psi^2(\mathbf{x}, \tau) + \psi^3(\mathbf{x}, \tau) \right. \\ & \left. - \beta \int d^d x' g(|\mathbf{x} - \mathbf{x}'|) \psi(\mathbf{x}', \tau) \right] + \sqrt{\epsilon} \mu(\mathbf{x}, \tau), \end{aligned} \quad (8)$$

where

$$\langle \mu(\mathbf{x}, \tau) \mu(\mathbf{x}', \tau') \rangle = (-\nabla^2)^n \delta(\mathbf{x} - \mathbf{x}') \delta(\tau - \tau'),$$

$$q_c^2(\tau) = 1 - 3\overline{\psi(\tau)^2},$$

$$\alpha g(|\mathbf{r} - \mathbf{r}'|) = \frac{\alpha}{r} \left( \frac{\kappa}{r} \right)^{\frac{d-1}{2}} g(|\mathbf{x} - \mathbf{x}'|) = \beta g(|\mathbf{x} - \mathbf{x}'|)$$

and

$$\epsilon = \frac{k_B T u}{r^2} \left( \frac{r}{\kappa} \right)^{d/2}. \quad (9)$$

For MB<sub>L</sub>  $\overline{\psi(\tau)} = \psi_0 = \left(\frac{u}{r}\right)^{\frac{1}{2}} \phi_0 = \text{const}$  so  $q_c^2(\tau)$  is also independent of time. Equation (8) describes the time evolution of the order-parameter *fluctuations*. This is the only relevant equation for MB<sub>L</sub>. For MA<sub>L</sub> Eq. (8) is augmented by an equation describing the time variation of the average order parameter

$$\frac{\partial \overline{\psi(\tau)}}{\partial \tau} = \frac{1}{2} [(1 - \beta L) \overline{\psi(\tau)} - \overline{\psi(\tau)^3} + h],$$

where

$$h = \left( \frac{u}{r} \right)^{\frac{1}{2}} \frac{H}{r}. \quad (10)$$

The function of the field therefore is to produce and maintain a net overall magnetization  $\overline{\psi(\tau)}$  which rapidly reaches equilibrium and remains constant so that the subsequent dynamics is governed solely by Eq. (8).

The stochastic integro-differential equation described by the Eqs. (8)–(10) is characterized by five dimensionless parameters: the off criticality  $\psi_0$ , which defines the asymmetry between the two phases ( $\psi_0 = 0$  implies a symmetric 50-50 mixture,  $\psi_0 = 0.2$  implies a 60-40 mixture, etc.); the external field  $h$ ; the relative strength of the LRRI  $\beta$ ; and the strength of the thermal noise  $\epsilon$ . As shall be discussed, the LRRI kernel  $g(|\mathbf{x} - \mathbf{x}'|)$  depends on a dimensionless layer thickness  $L = l \left(\frac{r}{\kappa}\right)^{\frac{1}{2}}$ . Note that in the absence of a LRRI (i.e.,  $\beta = 0$ ), these equations reduce to those of model B or model A, depending upon whether the order parameter is conserved or not.

Note that experimental quenches where the temperature is varied can be mapped into our model. From the equations above,  $\beta = \frac{\alpha \kappa^{(d-1)/2}}{r^{(d+1)/2}}$ , where  $r \sim (T_c - T) > 0$ . For most experimental systems the strengths of the LRRI  $\alpha$  and of the short-range attractive force  $\kappa$  are fixed. The LRRI suppresses the fluctuations near  $T_c$  so the onset of the modulated patterns occurs for a temperature slightly lower than  $T_c$  (in a single-mode approximation of wave number  $k_{SM}$ ), the new ordering temperature  $T_0$  is given by  $T_0 = T_c (1 - k_{SM}^2 - \beta g(k_{SM}))$ . Near this ordering temperature,  $r$  reaches its minimum value  $r = r_c > 0$  and  $\beta$  its maximum  $\beta = \beta_c$ . As the temperature is lowered,  $r$  increases and  $\beta$  decreases. Quenches for high temperatures (shallow quenches) are mimicked in our simulations

by quenches with high  $\beta$  while quenches for low temperatures (deep quenches) are mimicked by quenches with low  $\beta$ . In this way  $\beta$  controls the depth of the quench while the noise term accounts for the thermal fluctuations.

In order to complete the description of the problem, the form of the kernel describing the LRRI,  $g(|\mathbf{x} - \mathbf{x}'|)$ , must be specified. This will, of course, depend upon the specific system under consideration. In this paper we consider the case of a uniaxial ferromagnetic film and that of a monomolecular film of phospholipid monolayer confined to an air-water interface.

Consider the case of a uniaxial ferromagnetic film of thickness  $L$ . In the  $xy$  plane, the film is assumed to be large and isotropic (in the disordered phase). If the film is strongly uniaxial, one can assume straight domain walls in the vertical ( $\hat{z}$ ) direction, so that the film may be treated as a two-dimensional system. The order parameter is taken to be the magnetization averaged over the vertical direction. The external magnetic field  $h$  is also assumed to be oriented in the vertical direction.

This system is characterized by a balance between domain-wall energy and its magnetostatic self-energy: the system can reduce the latter by forming domains of ordered phases at the cost of introducing domain walls between the phases. If the system contains  $N$  domains, its free energy is about  $1/N$  times lower than that of a uniformly magnetized film. Hence the formation of modulated structures is favored. Since the magnetization is not conserved, MA<sub>L</sub> is appropriate for the description of this system. For this case, the LRRI is given by

$$g(|\mathbf{x} - \mathbf{x}'|) = \frac{1}{|\mathbf{x} - \mathbf{x}'|} - \frac{1}{[(\mathbf{x} - \mathbf{x}')^2 + L^2]^{\frac{3}{2}}}$$

$$= \int d\mathbf{k} \frac{(1 - e^{-Lk})}{k} e^{i\mathbf{k} \cdot (\mathbf{x} - \mathbf{x}')}, \quad (11)$$

with a strength  $\alpha \sim (g\mu_B)^2$ , where  $g\mu_B$  is the appropriate gyromagnetic coefficient of the material [4]. Notice that for  $|\mathbf{x} - \mathbf{x}'|$  large compared to  $L$ ,  $g(|\mathbf{x} - \mathbf{x}'|)$  approaches  $L^2/(2|\mathbf{x} - \mathbf{x}'|^3)$ , which is like a repulsive dipolar kernel.

The formation of domains in monomolecular films of phospholipids confined to an air-water interface (Langmuir monolayers) is equivalent in its main features to the domain formation in the uniaxial ferromagnetic films. Specifically, the short-range interactions between the long-chain molecules is the source of the short-range attractive interfacial (domain-wall) energy, in the sense of van der Waals and Landau. This is balanced by a nonlocal repulsive term arising from the normal component of the dipolar (electrostatic) forces between the polar heads of these molecules. The free energy contributed by this interaction is reduced by spatial modulations in the pertinent order-parameter field, which is the lateral molecular density in single-component films or the intralayer concentration in binary mixtures. Thus we can use the same model kernel as in Eq. (11) above to describe in a simplified manner these two-dimensional amphiphilic films. Since the number of molecules is conserved, we require the conservation law as in MB<sub>L</sub> to describe the corresponding dynamics.

### III. PHASE DIAGRAM

Equilibrium phase diagrams for a dipolar lattice gas [17], for a uniaxial ferromagnetic film (see last reference in [4]), and for Langmuir monolayers [18] have previously been studied. We have extended the single-mode studies to an arbitrary number of modes to obtain the zero-temperature phase diagram. For fixed values of  $L$  and  $\beta$ , modulated stripe and hexagonal disk patterns are formed as function of the external field  $h$  ( $MA_L$ ) or of the off criticality  $\psi_0$  ( $MB_L$ ). The equilibrium states of the system are obtained by studying the solutions of  $\frac{\delta F}{\delta \psi} = 0$ . In equilibrium, the coefficients of the Fourier expansion do not depend on time. We can write the equilibrium order parameter as

$$\psi(\mathbf{x}) = \bar{m} + \sum_{\mathbf{k}} e^{-i\mathbf{k}\cdot\mathbf{x}} m_{\mathbf{k}}, \quad (12)$$

where  $\bar{m}$  is the average overall concentration ( $= \psi_0$  for  $MB_L$  and  $= \overline{\psi(\tau = \infty)}$  for  $MA_L$ ) and the zero wave vector Fourier component  $m_{\mathbf{0}} = 0$ . A few geometrical properties of the lattice allow us to make some simplifications in this expansion. Since  $\psi(\mathbf{x})$  is real and the lattice has inversion symmetry,  $m_{-\mathbf{k}} = m_{\mathbf{k}}$ . Furthermore, since all the neighbors at an equal distance from a given stripe or disk are indistinguishable,  $m_{\mathbf{k}}$  only depends on the modulus of  $\mathbf{k}$  and we write  $m_{\mathbf{k}} = m_k$ . Thus we can write

$$\sum_{\mathbf{k}} e^{-i\mathbf{k}\cdot\mathbf{x}} m_{\mathbf{k}} = \sum_{|\mathbf{k}|} m_k \sum_{\hat{k}} e^{-i\mathbf{k}\cdot\mathbf{x}}, \quad (13)$$

where  $\sum'_{\hat{k}}$  means sum over all those vectors  $\mathbf{k}$  such that  $|\mathbf{k}| = k$  and  $\sum'_{\hat{k}} = n_k$  is the number of those vectors. With this convention,  $\frac{\delta \psi(\mathbf{x})}{\delta m_k} = \sum'_{\hat{k}} e^{-i\mathbf{k}\cdot\mathbf{x}}$  and the functional derivative  $\frac{\delta F}{\delta \psi}$  becomes

$$\begin{aligned} \frac{1}{A} \frac{\delta F_i}{\delta m_k} = & -[q_c^2 - k^2 - \beta g(k)] m_k n_k \\ & + 3\bar{m} \sum_{\mathbf{k}'} \sum_{\hat{k}} m_{\mathbf{k}'} m_{|\mathbf{k}+\mathbf{k}'|} \\ & + \sum_{\mathbf{k}'} \sum_{\mathbf{k}''} \sum_{\hat{k}} m_{\mathbf{k}'} m_{\mathbf{k}''} m_{|\mathbf{k}+\mathbf{k}'+\mathbf{k}''|}, \end{aligned} \quad (14)$$

where  $A$  is the area of the system,  $q_c^2 = 1 - 3\bar{m}^2$ , and the subscript  $i$  stands for  $S$  (stripe) or  $H$  (hexagonal). The problem consists of solving the set of coupled equations  $\frac{\delta F_i}{\delta m_k} = 0$  and the corresponding equation for the minimization of the wave number  $k$ . For the hexagonal phase,  $k = k_{\text{eq}} \sqrt{n_1^2 + n_1 n_2 + n_2^2}$  and  $k_{\text{eq}} = \frac{4\pi}{\sqrt{3}a}$ , where  $a$  is the lattice constant and  $n_1, n_2$  are integers [the pairs  $(0, 1)$ ,  $(1, 0)$ ,  $(1, -1)$ , and their symmetrical counterparts give the sixfold Bragg peak].

In principle, Eq. (14) consists of an infinite number of coupled equations, which need to be truncated and solved numerically [19]. The number of harmonics needed depends on  $\beta$ : for small  $\beta$  we need to include more harmonics as the limit for  $\beta \rightarrow 0$  corresponds to a square well profile, while for  $\beta \leq \beta_c$ , even a few harmonics are enough. (Very near  $\beta_c$ , the single-mode approximation is excellent.) Once we get  $\psi(\mathbf{x})$  expressed in its Fourier components, we substitute its expression in the free-energy functional form and use the double tangent construction to get the different regions in our phase diagram. We look for the absolute minimum of  $F_i - \mu \bar{m}$ , where  $F_i = F_S, F_H$ , or  $F_I$  (the subscript  $I$  stands for the isotropic phase) and  $\mu$  is the chemical potential or the magnetic field magnitude coupled to the average concentration  $\bar{m}$ .

Figure 1 shows the phase diagram in the  $(\beta, \bar{m})$  plane for  $L = 10$ . Here  $\bar{m}$  is a constant and equal to  $\psi_0$  for  $MB_L$  or is the average overall magnetization produced by the field in  $MA_L$  (the field  $h = 0.33$  mostly used in our simulations gives an overall concentration  $\bar{m} = 0.23$  in equilibrium). Data for  $\beta < 0.03$  are based on extrapolation due to numerical difficulties in this parameter regime. Moving from  $\bar{m} = 0$  to greater values of  $|\bar{m}|$  for a fixed  $\beta$ , we

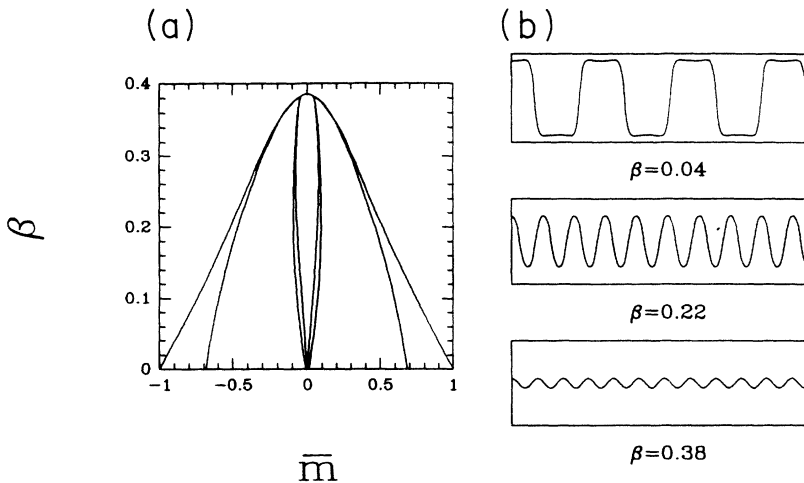


FIG. 1. For  $L = 10$ , (a) shows the phase diagram in the  $(\beta, \bar{m})$  plane and (b) shows profiles of the order parameter for  $\bar{m} = 0$  (or  $\psi_0 = 0$  and  $h = 0$ ) for different values of  $\beta$ .

find the central region corresponding to the stripe phase, an area of stripe-hexagonal coexistence, the hexagonal phase, an area of hexagonal-isotropic coexistence, and the isotropic phase. In our system, the hexagonal phase corresponds to what is called a “low-density” phase, in which the disks are always the minority phase (i.e., their total area is less than 50% of the total area); some other more complex systems can show a high-density phase, from 50% up to 92%, corresponding to closest circular packing. For the point at  $\bar{m} = 0$  where the stripe phase meets the isotropic phase, we found a value of  $\beta_c = 0.385$ . For a slab of finite thickness, the dipolar coupling is always found to be relevant, so that the ground state of the system remains modulated for all values of  $\beta$ . Only on the line  $\beta = 0$ , we recover the Ginzburg-Landau free-energy result. Figure 1 also shows the profiles of the order parameter for the symmetric stripe phase. From these pictures, we see that as  $\beta \rightarrow 0$ , the profile approaches a square well, its amplitude increases towards unity, and its characteristic wavelength becomes progressively longer. (The amplitude corresponding to  $\beta = 0$  is precisely unity and its wavelength is infinite.) As  $\beta \rightarrow \beta_c$ , on the other hand, the profile looks more and more sinusoidal, while the amplitude and the characteristic wavelength continuously diminish. Figure 2(a) shows the predicted variation of the saturation value of the order parameter  $\psi_{\text{sat}}$  with the strength  $\beta$  of the LRRI.

Figure 2(b) compares the equilibrium wave number  $k_{\text{eq}}$  of the system with two commonly used approximations.

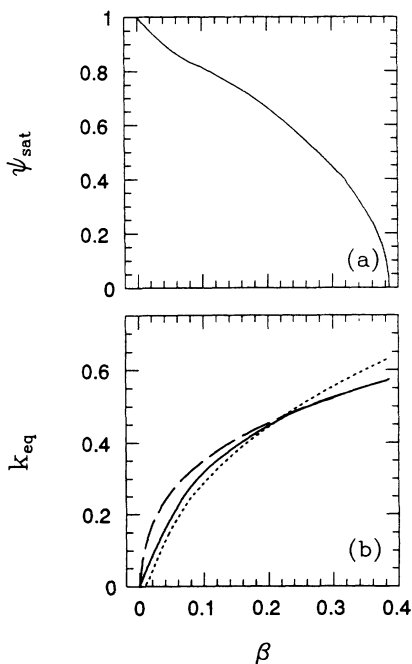


FIG. 2. (a) shows the variation of the amplitude of the order parameter for  $L = 10$ ,  $\bar{m} = 0$  with  $\beta$ . For the previous parameters, (b) shows the equilibrium wave number  $k_{\text{eq}}$  that results from our calculation (solid line), the single-mode approximation to the equilibrium wave number  $k_{\text{SM}}$  (long-dashed line), and the hard-wall approximation to the equilibrium wave number  $k_{\text{HW}}$  (dotted line).

The simplest possible approximation is the single-mode approximation, in which the modulation of the order parameter is given by  $\psi_{\text{SM}} \sim \cos(k_{\text{SM}}x)$  and  $k_{\text{SM}}$  is given by the solution of

$$\frac{df_k}{dk} = -\frac{1}{2} \frac{d}{dk} \left[ \beta \frac{1 - e^{-kL}}{k} + k^2 \right]_{k=k_{\text{SM}}} = 0. \quad (15)$$

The other common approximation is the hard-wall approximation, in which the corresponding equilibrium wave number  $k_{\text{HW}}$  is given as the solution of

$$\frac{d}{dk} \left[ k + \beta \sum_{n=0}^{\infty} \frac{1}{(2n+1)^3} \frac{(1 - e^{-(2n+1)kL})}{k} \right]_{k=k_{\text{HW}}} = 0. \quad (16)$$

The competing effects of attractive and repulsive interactions determine not only the stability of the shapes of individual domains, but also the dynamics of domain-wall fluctuations and shape transitions. For many of the relevant physical systems, the domains can exhibit a variety of shapes which are not always equilibrium shapes. For uniaxial ferromagnetic films, the stability to harmonic distortions has been studied for disks and stripes [4], where the circular shape has been shown to undergo an elliptical instability; however, higher-harmonic shapes are not so important. The “stripe-hexagonal” transition is hindered by a surface energy barrier that must be overcome in the conversion process. This is the origin of the topological hysteresis which is related not to wall pinning by defects but to nucleation and collapse field problems [20]. Theoretical calculations in thin layers of ferrofluids [6] and Langmuir films [21] have shown instabilities not only to elliptic shapes but also to higher-harmonics shapes which have been found experimentally [22,23]. Seul and co-workers have identified in amphiphilic monolayers, the presence of an elliptic instability, and a branching instability leading to a melted stripe phase near the consolute point. But while ferromagnetic films and ferrofluid layers follow an essentially deterministic dynamics, Langmuir films are very sensitive to thermal fluctuations and cannot be described by mean-field treatments, except in the  $T = 0$  limit. Furthermore, while in the case of ferromagnets the LRRI can be approximated by a local Hamiltonian described by a curvature elastic energy, the behavior in the monolayers can be more accurately described by an effective local capillary-wave Hamiltonian. In this paper we only deal with dynamics following quenches from the disordered state, leaving the interesting “stripe-hexagonal” transition for future study.

#### IV. INITIAL STAGES OF THE DYNAMICS

As stated in the Introduction, the process of phase separation involves the simultaneous segregation into two phases and creation of a supercrystal ordering. These processes involve very different time scales. In the early and intermediate stages, the processes related to phase

segregation and formation of domains are predominant. At late times the domains are essentially monodisperse and the process of ordering dominates. In the early time regime, the instability amplifies the fluctuations present in the initial conditions, saturates them, and forms sharp interfaces. This early time regime is dominated by  $k_m$ , the maximally unstable wave number of the linear dispersion relation. During this time, the amplitude of the order parameter grows towards its saturation value. In contrast, the intermediate time regime is dominated by the wave number of the equilibrium modulated structure  $k_{\text{eq}}$ . The characteristic time of this regime is the time that the domains require to reach their equilibrium wavelength  $2\pi/k_{\text{eq}}$ . Thus the dynamics of this stage involves crossover phenomena, as the characteristic wave number of the system changes from  $k_m$  to  $k_{\text{eq}}$ . Immediately after the quench, the system acquires a very complicated morphology of irregular interpenetrating domains that percolate through the system. As time evolves these domains either evolve towards their eventual stripe shape, or neck, and pinch away to form individual clusters for an eventual hexagonal lattice morphology. During the intermediate time regime, the domains become progressively more regular (the stripes become smoother and more rectangular and the individual clusters become more circular). The crossover from  $k_m$  to  $k_{\text{eq}}$  is achieved by varying the number of domains (for instance, for  $\text{MB}_L$  where  $k_m > k_{\text{eq}}$  the number of domains in the hexagonal phase can be reduced by coalescence of two disks because this process increases the characteristic length of the periodicity). Eventually the number of domains stays essentially constant and the distribution function of the stripe width or the disk radii becomes highly peaked around the equilibrium value. By this time, the shape transition processes are nearly complete and the system has become a monodisperse disordered liquid of either stripes or disks. This marks the onset of the late-time regime. This late stage of phase ordering involves the evolution from this disordered liquid towards the crystalline ground state through the gain of orientational and positional order. The main mechanism of this ordering process is collision and annihilation of defects. The actual achievement of crystalline order in the late stage can depend on several factors, such as the depth of the quench (or, equivalently, the strength of the dipolar interactions), the presence of noise, etc.

We sum up as follows. The early-time regime corresponds to the amplification of the initial fluctuations and the saturation of the order parameter, the intermediate-time regime corresponds to the processes associated with the geometrical degrees of freedom of the system, and the late stage corresponds to the processes associated with the topological degrees of freedom. For  $\text{MA}_L$  this distinction is quite sharp. For example, in run  $F$  (see Table I), the saturation is reached at  $\tau \sim 30$ , after  $\tau = 200$  the number and radii of disks stays constant, while the topological stage extends to  $\tau \sim 20\,000$ . The geometrical degrees of freedom are completely decoupled from the topological ones. For  $\text{MB}_L$ , this distinction is only an approximation. As a consequence of the conservation law, the geometrical degrees of freedom never really decou-

TABLE I. Parameters used in simulation.  $n_{\text{run}}$  is the number of independent quenches.

Run	Model	$L$	$\beta$	$\psi_0$	$h$	$n_{\text{run}}$
$A$	$\text{MB}_L$	10	0.22	0.0	0.0	5
$B$	$\text{MB}_L$	0.1	5	0.0	0.0	5
$C$	$\text{MB}_L$	10	0.22	0.2	0.0	5
$D$	$\text{MB}_L$	0.1	5	0.2	0.0	5
$E$	$\text{MA}_L$	10	0.22	0.0	0.0	5
$F$	$\text{MA}_L$	10	0.22	0.0	0.33	5

ple from the topological ones. In the intermediate time, most of the crossover phenomena and the achievement of the characteristic geometry occurs, but at late time these processes still continue (though very slowly) and isolated coalescence events still contribute to the achievement of crystalline order. For run  $C$ , the saturation is reached at  $\tau \sim 200$  while the curve of the lattice constant versus time reaches an approximate plateau at  $\tau \sim 2000$ ; however, there are still coalescence events at late times indicating that the system has not yet reached the equilibrium modulation  $k_{\text{eq}}$ .

During the early and intermediate-time regime, all the necessary information about the system is directly obtained from the scalar order parameter. During the intermediate regime, the domain size reaches a time-independent value: since the time evolution is ultimately governed by this length scale, the system does not display scaling in the equal-time two-point correlation function of the scalar order parameter. For the late stage, when crystalline ordering process dominates the evolution, the system can be described by measuring the way in which correlations decay (exponential, algebraic) and the length over which they decay, as well as the development of twofold or sixfold symmetry in the structure factor. For this purpose it is very useful to describe the ordering process in terms of two vector order parameters, constructed from the original scalar order parameter: an orientational and a translational order parameter. The new characteristic length scales of the late stage evolution are related to the size of the ordered regions. Since the free energy of the modulated system is degenerate with respect to the direction of  $\mathbf{k}_{\text{eq}}$ , a quench from the disordered phase into the ordered one results in the formation of modulated phase broken up by defects (disclinations and dislocations). The new length scales grow at a characteristic rate as different broken symmetry phases compete to select the ground state. Although computation limitations prevented us to study the scaling in the correlation function or structure factor of the two vector order parameters, for large systems and times long enough one should expect scaling in these quantities.

To analytically study the equation of motion, Eq. (8), it is convenient to transform it into Fourier space. The order parameter then becomes

$$\psi(\mathbf{x}, \tau) = \sum_{\mathbf{k}} e^{-i\mathbf{k}\cdot\mathbf{x}} \psi_{\mathbf{k}}(\tau) = \psi_0(\tau) + \sum_{\mathbf{k} \neq 0} e^{-i\mathbf{k}\cdot\mathbf{x}} \psi_{\mathbf{k}}(\tau) \quad (17)$$

[where  $\psi_0(\tau) = \overline{\psi(\tau)}$ ], and Eq.(8) is transformed into

$$\frac{\partial \psi_{\mathbf{k}}(\tau)}{\partial \tau} = \gamma_{\mathbf{k}} \psi_{\mathbf{k}}(\tau) - \frac{(k^2)^n}{2} \left[ 3\psi_0(\tau) \sum_{\mathbf{k}'} \psi_{\mathbf{k}'}(\tau) \psi_{\mathbf{k}-\mathbf{k}'}(\tau) + \sum_{\mathbf{k}'} \sum_{\mathbf{k}''} \psi_{\mathbf{k}'}(\tau) \psi_{\mathbf{k}''}(\tau) \psi_{\mathbf{k}-\mathbf{k}'-\mathbf{k}''}(\tau) \right] + \sqrt{\epsilon} \mu_{\mathbf{k}}, \quad (18)$$

with a linear dispersion relation

$$\gamma_{\mathbf{k}} = \frac{(k^2)^n}{2} [q_c^2 - k^2 - \beta g(k)], \quad (19)$$

where  $g(k)$  is the  $d$ -dimensional Fourier transform of  $g(x)$  and the dependence of  $q_c^2$  on time can be neglected.

We can linearize this equation and solve for the linear structure factor, valid for very early times. First we note that the post-quench value of the structure factor is the corresponding stationary solution for the structure factor in the single-phase region of the phase diagram [where  $f(\phi) = \frac{r_0}{2}\phi^2 + \frac{u}{4}\phi^4$ ,  $r_0 > 0$ ] and which has the modified Ornstein-Zernike form. Thus at time  $\tau = 0^+$ , the structure factor is

$$\langle |\psi_{\mathbf{k}}(0)|^2 \rangle = \frac{\epsilon_I}{q_c^2 + k^2 + \beta g(k)}, \quad (20)$$

where  $\epsilon_I = \frac{\epsilon}{(2\pi)^d} \frac{T_i r_0^{2-d/2}}{T_f r_0^{2-d/2}}$ . Here  $T_i$  and  $T_f$  represent the initial and final quench temperatures, respectively.

Linearizing Eq. (18) and introducing the two-point correlation function

$$\langle \psi_{\mathbf{k}}(\tau) \psi_{\mathbf{k}'}(\tau) \rangle = \delta(\mathbf{k} + \mathbf{k}') \langle |\psi_{\mathbf{k}}(\tau)|^2 \rangle, \quad (21)$$

one readily obtains the linear structure factor

$$\langle |\psi_{\mathbf{k}}(\tau)|^2 \rangle = \langle |\psi_{\mathbf{k}}(0)|^2 \rangle e^{2\gamma_{\mathbf{k}} \tau} + \frac{(k^2)^n \epsilon}{(2\pi)^d} \left[ \frac{e^{2\gamma_{\mathbf{k}} \tau} - 1}{2\gamma_{\mathbf{k}}} \right]. \quad (22)$$

The dispersion relation [Eq. (19)] for the LRR1 given in Eq. (11) is

$$\gamma_{\mathbf{k}} = \frac{1}{2} (k^2)^n \left[ q_c^2 - k^2 - \beta(1 - e^{kL})/k \right], \quad (23)$$

which for small  $k$  reduces to

$$\gamma_{\mathbf{k}} = \frac{1}{2} (k^2)^n \left[ (q_c^2 - \beta L) + \frac{1}{2} \beta L^2 k - \left( 1 + \frac{\beta L^3}{6} \right) k^2 + O(k^3) \right]. \quad (24)$$

Consider the three terms in square brackets. The presence of LRR1 alters the coefficient of  $(-k^2)$  from 1 to  $(1 + \beta L^3/6)$ , which corresponds to a renormalization of the surface tension. Similarly the constant term is altered from  $q_c^2$  to  $(q_c^2 - \beta L)$ , renormalizing the harmonic term of the bulk free energy. The second term  $\frac{1}{2} \beta L^2 k$  is the direct consequence of LRR1. [Note that the two-dimensional Fourier transform of the dipolar interaction kernel  $g(x) \sim 1/x^3$  is  $g(\mathbf{k}) \sim -|\mathbf{k}|$ .] It competes with the third term, arising from the renormalized square-gradient interaction and leads to modulated structures as the sys-

tem evolves. For  $\beta = 0$ , the system is characterized by growing domains which coarsen via  $\tau^{\frac{1}{3}}$  for model B and  $\tau^{\frac{1}{2}}$  for model A. In both cases, the morphology is self-similar at late times. This is qualitatively different from the modulated structures that one gets for  $\beta > 0$ .

From Eqs. (22) and (23), it is clear that the initial growth of the pattern is determined by the linear dispersion  $\gamma_{\mathbf{k}}$ . The system is unstable with respect to fluctuations of modes  $k$  such that  $\gamma_{\mathbf{k}} > 0$  and stable with respect to fluctuations of mode  $k$  such that  $\gamma_{\mathbf{k}} < 0$ . Using Eq. (23), the maximally unstable mode  $k_m$  is easily found. We shall write  $\gamma_m = \gamma(k_m)$ . The presence of  $\beta > 0$  decreases  $\gamma_m$  and shifts the maximally unstable mode: from  $k = 0$  to  $k > 0$  for MA<sub>L</sub> and from  $k = 1/\sqrt{2}$  to  $k < 1/\sqrt{2}$  for MB<sub>L</sub>. For small values of  $kL$ , we can use Eq. (24) to find the roots of  $\gamma_{\mathbf{k}} = 0$ . If  $(\beta L - q_c^2) \leq 0$ , there exists only one positive real root  $k_{02}$ . For MA<sub>L</sub>, the  $k = 0$  mode is still unstable and in the point where  $\beta L = q_c^2$  the dispersion relation is  $\gamma_0 = 0$ . For MB<sub>L</sub>, the  $k = 0$  mode is fixed and marginally stable due to the conservation law. If, on the other hand,  $0 < (\beta L - q_c^2) < \frac{1}{16} \beta^2 L^4 / (1 + \beta L^3/6)$ , there are two positive real roots; the  $k = 0$  mode is stable for MA<sub>L</sub> and marginally stable for MB<sub>L</sub>. The dispersion relation presents a band of stable modes,  $0 < k < k_{01}$ , and then a band of unstable modes,  $k_{01} < k < k_{02}$ . However, as  $L$  decreases, the root  $k_{01}$  approaches zero; if  $\beta L > q_c^2$  and  $L < 1$ , the band of unstable modes is negligible. For all practical quenches, systems with  $L < 1$  only exhibit a band of unstable modes for  $(\beta L - q_c^2) \leq 0$ . Figure 3 shows the  $k$  dependence of the dispersion relation  $\gamma_{\mathbf{k}}$  for MB<sub>L</sub> and MA<sub>L</sub> for  $L = 10$  and  $L = 0.1$  for a critical quench with no field and for different values of  $\beta$ .

The two characteristic time scales in the initial stages of the evolution are  $\tau_m$  and  $\tau_e$ . Here  $\tau_m$  is the saturation time (i.e., the time that it takes the order parameter to reach its saturation value) and  $\tau_e$  is the geometrical time (i.e., the time that it takes the domains to reach their equilibrium saturation wavelength  $\frac{2\pi}{k_{eq}}$ ). These characteristic times depend on the presence or absence of the conservation law and on the parameters  $L$ ,  $\beta$ , and  $\psi_0$  (or the field  $h$  through  $\bar{m}$ ). Due to the absence of a conservation law, the dynamics of MA<sub>L</sub> is much faster than that of MB<sub>L</sub>. The value of  $\tau_m$  is given by  $\tau_m \sim \gamma_m^{-1}$ . For a given  $L$ , it decays monotonically with either decreasing  $\beta$  at fixed  $\bar{m}$  or with decreasing  $\bar{m}$  at fixed  $\beta$ ; for a fixed  $\bar{m}$  and  $\beta$ , it is larger for decreasing  $L$ . Figure 4(a) shows the dependence of  $\tau_m$  on the different set of parameters. For certain combinations of these parameters,  $\tau_m$  diverges near a critical value of  $\beta L$ . This is due to the fact that the system is approaching the new effective spinodal line. The value of  $\tau_e$  depends on the difference  $\Delta k = k_m - k_{eq}$  (which obviously depends on the mentioned parameters). The crossover phenomenon from the stage where the dynamics are governed by  $k_m$  to when they are governed by  $k_{eq}$  is common to MA<sub>L</sub>

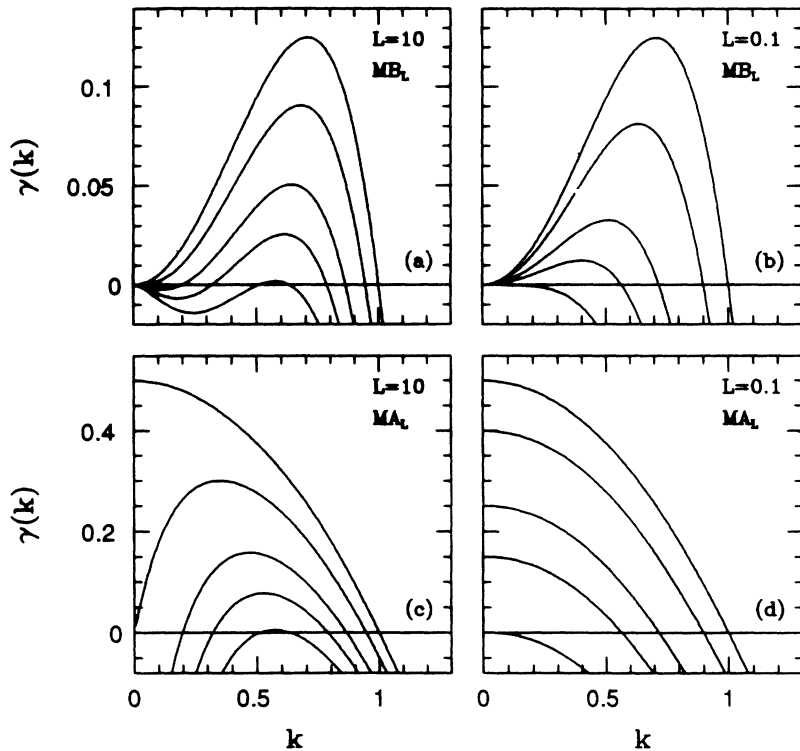


FIG. 3. Dependence of the dispersion relation  $\gamma(k)$  on the wave number  $k$  for critical quenches. From top to bottom, (a) and (c) show the curves for the thick film ( $L = 10$ ) for  $\beta = 0, 0.1, 0.22, 0.30,$  and  $0.38$ ; (b) and (d) show the curves for the thin film ( $L = 0.1$ ) for  $\beta = 0, 2, 5, 7,$  and  $10$ .

and  $MB_L$ . In  $MA_L$  the maximally unstable wave mode  $k_m$  coincides with the equilibrium wave mode  $k_{SM}$  computed in a single-mode approximation so the difference  $\Delta k = k_m - k_{eq}$  is relatively small. In the simulations for  $MA_L$ , the system takes relatively short time ( $\tau_e \sim 200$  for the hexagonal phase,  $L = 10, \beta = 0.22$ ) to reach its equilibrium modulation length scale. However, in  $MB_L$  the maximally unstable wave mode is quite far from the equilibrium wave mode, and this large gap  $\Delta k$  causes the system to take much longer time to reach its equilibrium period. Although the curve of the lattice spacing with time seems to reach a plateau about  $\tau_e \sim 2000$  (for  $L = 10, \beta = 0.22,$  and  $\psi_0 = 0.2$ ), still at very late times one can see in the hexagonal phase coalescence of two domains, indicating that the lattice constant is growing very slowly. Besides, for both models,  $\Delta k$  is larger for systems with  $\beta L < q_c^2$  (particularly those with  $L < 1$ ). These sys-

tems have very large equilibrium periods (whether stripe widths or disk radii) and the system takes much longer to reach the stage of the single dominant equilibrium wavelength. Figure 4(b) shows the equilibrium wave number  $k_{eq}$  and maximally unstable wave number  $k_m$  for  $MB_L$  for  $\psi_0 = 0$  and  $0.4$  ( $L = 10, \beta = 0.22$ ). In Fig. 2(b), the equilibrium single mode  $k_{SM}$ , which is also the unstable wave mode  $k_m$  for  $MA_L$ , is compared to the true equilibrium wave number  $k_{eq}$  and with the hard-wall approximation  $k_{HW}$ .

While the linear analysis is useful in identifying the unstable modes initially, the linear solution incorrectly predicts an unbounded, exponential growth of the order parameter for these wave numbers. Such a solution can only be valid for very early times [1]. To temper the exponential growth, the nonlinearities must be taken into account. For model A, a successful theory was formulated

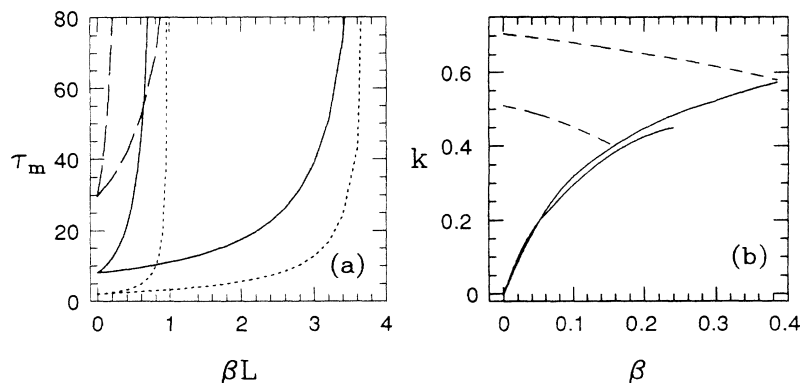


FIG. 4. (a) shows  $\tau_m$  computed as the inverse of the maximum of the dispersion relation. The dotted lines correspond to  $MA_L$  with  $h = 0$ , the solid lines correspond to  $MB_L$  with  $\psi_0 = 0$ , and the long-dashed lines correspond to  $MB_L$  with  $\psi_0 = 0.4$ . In every pair of lines, the left line corresponds to  $L = 0.1$  and the right line to  $L = 10$ . (b) shows the equilibrium wave numbers  $k_{eq}$  (solid lines) and the maximally unstable wave number  $k_m$  for  $MB_L$  (dashed lines);  $L = 10$ . The longer lines correspond to  $\psi_0 = 0$  and the shorter lines correspond to  $\psi_0 = 0.4$ .

by Kawasaki, Yalabik, and Gunton (KYG) [24] which involves the resummation of an infinite number of terms in a singular perturbation expansion around the linear solution. This theory was extended for  $MA_L$  [13] and, as shown in the Appendix, may readily be formulated for  $MB_L$ . The predicted form for the order parameter is

$$\psi_{\mathbf{k}}(\tau) = \sum_{\mathbf{x}} e^{i\mathbf{k}\cdot\mathbf{x}} \psi^0(\mathbf{x}, \tau) \frac{(\alpha_k - 1)}{\sqrt{1+z}} \left(\frac{1+z}{z}\right)^{\alpha_k - 1} \times B_{\frac{z}{1+z}}\left(\frac{1}{2}\alpha_k - 1\right), \quad (25)$$

where  $B_x(a, b)$  is the incomplete beta function,  $z = \{k^2[\psi^0(\mathbf{x}, \tau)]^2\}/(2\gamma_m)$ , and  $\psi^0(\mathbf{x}, \tau)$  is the Fourier transform of  $\psi_{\mathbf{k}}^0(\tau) = e^{\gamma_{\mathbf{k}}\tau}\psi_{\mathbf{k}}(\tau = 0)$ .

In the next section, we give details of our simulations and compare the results with both the linear theory and the modified KYG solution.

## V. SIMULATION

### A. Numerical integration

The Langevin equation [Eq. (8)] was discretized using a standard finite-difference scheme [25]. The discretized equation was then integrated using both an Euler scheme, and a fourth-order Adams-Bashford predictor and an Adams-Moulton corrector technique [26]. We found that it was advantageous to use pseudospectral methods: the integral term was evaluated at each time instant by transforming  $\psi$  into  $k$  space, multiplying it by the discrete form of  $g(k)$ , and then transforming the product back into real space. It was found necessary to use an ‘‘isotropic’’ form of the Laplacian, which couples nearest- and next-nearest-neighbor cells.

The simulations reported in this paper were performed for two-dimensional  $64 \times 64$  and  $128 \times 128$  systems with periodic boundary conditions. The dimensionless mesh size  $\Delta x$  and the dimensionless time step  $\Delta\tau$  were chosen in such a way as to avoid possible spurious unphysical solutions resulting from the subharmonic bifurcation [25]. For the Euler scheme, we chose  $\Delta x = 1$  and  $\Delta\tau = 0.01$ . Using the predictor-corrector method, it was possible to use a larger time step of  $\Delta\tau = 0.1$ . For the hexagonal phase, we also simulated rectangular lattices. The ratio of lattice spacing  $\Delta x/\Delta y$  was kept at  $\sqrt{3}/2$  in order to accommodate an unstrained triangular array of disks.

We carried out simulations with different sets of parameters, in order to test different points in our phase diagram. Most of the results presented here come from  $128 \times 128$  square lattices for  $L = 10$  ( $MB_L$  and  $MA_L$ ) and for  $L = 0.1$  ( $MB_L$ ). In all cases the system was initially prepared in a homogeneous state by assigning a random number to each lattice site. The random numbers were uniformly distributed, with a mean value of  $\psi_0$  ( $\psi_0 = 0$  for  $MA_L$ ) and a width of 0.1 (the width of the distribution reflects the strength of thermal fluctuations in the initial state). Table I summarizes the parameters used in the simulation results described below.

### B. Quenches into the stripe phase

We now present numerical results for quenches from the disordered state into the stripe phase. Since a complete study of these quenches in  $MA_L$  was given in Ref. [13], here we shall only give results for  $MB_L$ . Systems with both stable and unstable long-wavelength modes are considered. The presence of thermal noise can affect (according to its strength) the final state of the system. Yet, for the study of the initial stages, it is not relevant, so we set  $\epsilon = 0$ .

Figures 5 and 6 show the time evolution of the order parameter morphology for systems corresponding to thick and thin layers (runs *A* and *B*, see Table I), respectively, at different times, as well as the order-parameter contours of an arbitrary cut through the system (the cut is shown as a horizontal line in each of the order-parameter morphology picture). The dark shading is used for regions of  $\psi > 0$  and the regions with  $\psi < 0$  are left unshaded.

Small inhomogeneities in the initial conditions are amplified by the band of unstable modes, giving rise to convoluted stripelike patterns broken up by disclinations and grain boundaries. These arise because the free energy of the system is degenerate with respect to the direction of the unstable modes. Therefore, in a quenched system, each point in the system selects an independent direction, which leads to a convoluted and interconnected pattern. Initially, the dynamics is dominated by short-ranged attractive forces, so that the early-time configurations are similar to early-time model B configurations. At early times isolated clusters of circular, oval, or similar irregular shape appear, most of which later disappear since the system is quenched to the stripe phase part of the equilibrium phase diagram. Later times are dominated by the LRRI, which limits the growth of the domains, building up stripelike patterns on short length scales. For the thick layer (Fig. 5, Run *A*), after  $\tau_e = 1000$ , the stripe thickness has remained essentially unchanged. The thin layer system shown in Fig. 6 (run *B*), on the other hand, has a much smaller equilibrium wave vector  $k_{eq}$ , so that at time  $\tau = 6000$  it is still growing in thickness.

To monitor the domain growth towards the equilibrium modulation length, we studied the amount of interfaces present in the system. Figure 7 shows the inverse perimeter density  $P$ , which is defined as the ratio of the total number of sites to the number of interface sites and is calculated as follows: any site with  $|\psi| \leq 0.75\psi_{sat}$  is counted as an interface site, otherwise, it is taken to be part of the bulk.

These pictures clearly indicate that systems with a complete band of initially unstable wavelength modes exhibit significant growth even for very long times. This is because for such systems  $k_{eq}$  is much smaller than  $k_m$ , so that after stripe patterns of period  $2\pi/k_m$  are formed at early times, on small length scales, these stripes begin to thicken and coarsen until they are of thickness  $2\pi/k_{eq}$ . For a system with stable long-wavelength modes, there is domain growth only in the early and intermediate stages. The growth is not self-similar and in contrast to model B ( $\beta = 0$ ), there is no late stage involving a self-similar

growth or a power-law time dependence of the domain size.

We computed the two-dimensional structure factor, which is

$$S(\mathbf{k}, \tau) = \left\langle \frac{1}{N^2} \left| \sum_{\mathbf{x}_i} \psi(\mathbf{x}_i, \tau) e^{i\mathbf{k} \cdot \mathbf{x}_i} \right|^2 \right\rangle, \quad (26)$$

where  $\mathbf{k} = (2\pi/N)(m\hat{\mathbf{i}} + n\hat{\mathbf{j}})$ ,  $m, n = 1, 2, \dots, N$ , where  $N$  is the system length. The circularly averaged structure factor is

$$S(k, \tau) = \sum_{\mathbf{k}} S(\mathbf{k}, \tau) / \sum_{\mathbf{k}} 1, \quad (27)$$

with  $k = 2\pi n/N$ ,  $n = 0, 1, 2, \dots, N$ , and the sum  $\sum_{\mathbf{k}}$  is over a circular shell defined by  $n - \frac{1}{2} \leq |\mathbf{k}|N/(2\pi) \leq n + \frac{1}{2}$ . We define the  $p$ th moment of the structure factor as

$$[k_p(\tau)]^p = \frac{\sum_{k=0}^{k_c} k^p S(k, \tau)}{\sum_{k=0}^{k_c} S(k, \tau)}. \quad (28)$$

$k_c$  is the cutoff frequency associated with the lattice. In our case,  $k_c = \frac{2\pi n_c}{L}$ , where we have chosen  $n_c$  to be the maximum possible value which is half the lattice size, i.e.,  $k_c = \pi$ . From the first moment of  $S(k, \tau)$ , one further measure of domain size can be defined as  $R_1(\tau) = \frac{2\pi}{k_1(\tau)}$ . Figure 8 shows the time evolution of  $R_1(\tau)$  for a thick layer as well as a thin layer and for both a symmetric ( $\psi_0 = 0$ ) and an asymmetric ( $\psi_0 = 0.2$ ) mixture. During the initial stages (considerably beyond the times when the linear theory is valid), the dynamics are dominated by shape changes. Comparing Figs. 5 and 6 to Fig. 8 one can see that shape changes at intermediate times correspond to the system acquiring a uniform thickness along

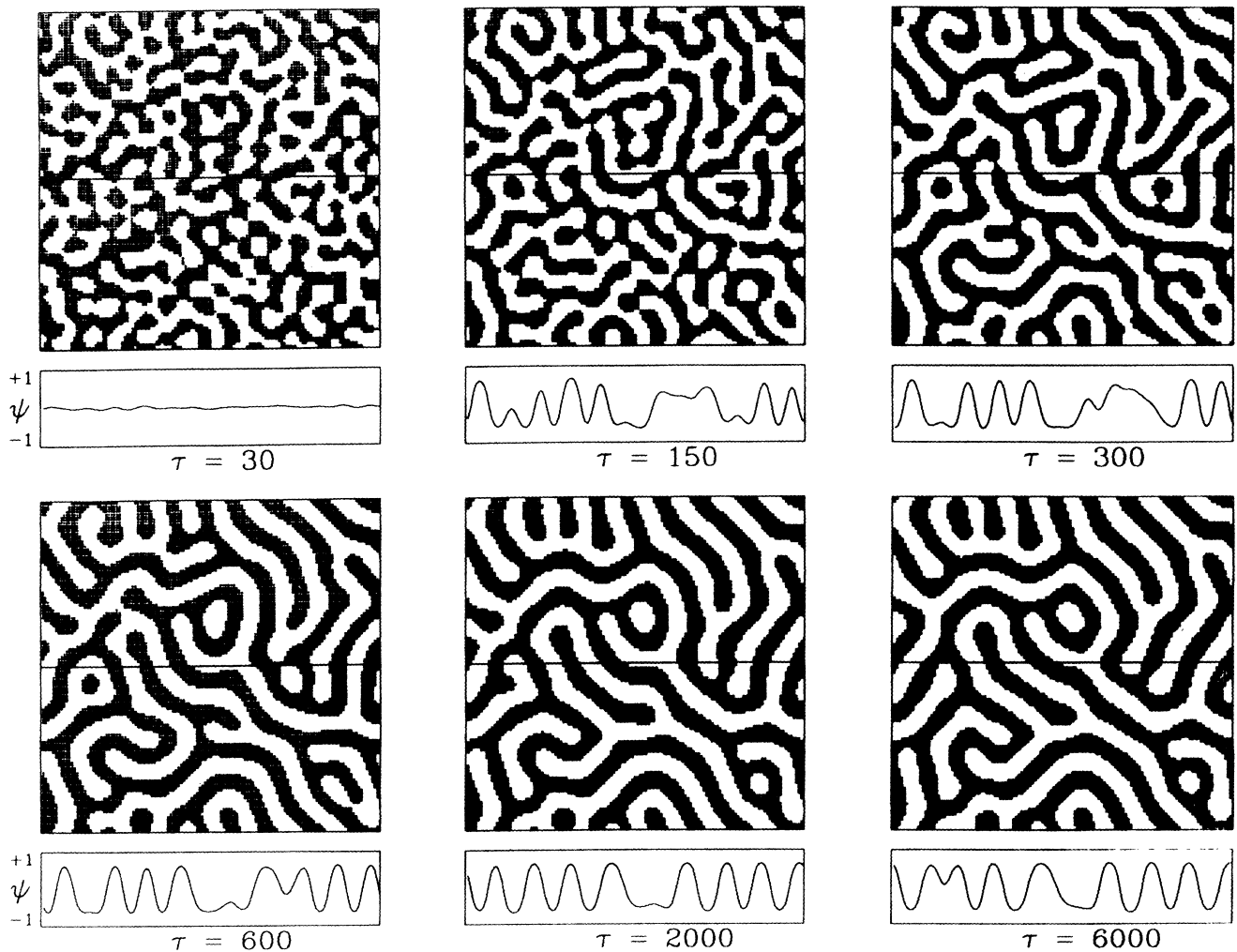


FIG. 5. Configuration pictures corresponding to  $MB_L$  for a critical quench in the thick film. (Run A:  $L = 10$ ,  $\beta = 0.22$ , and  $\psi_0 = 0$ .)

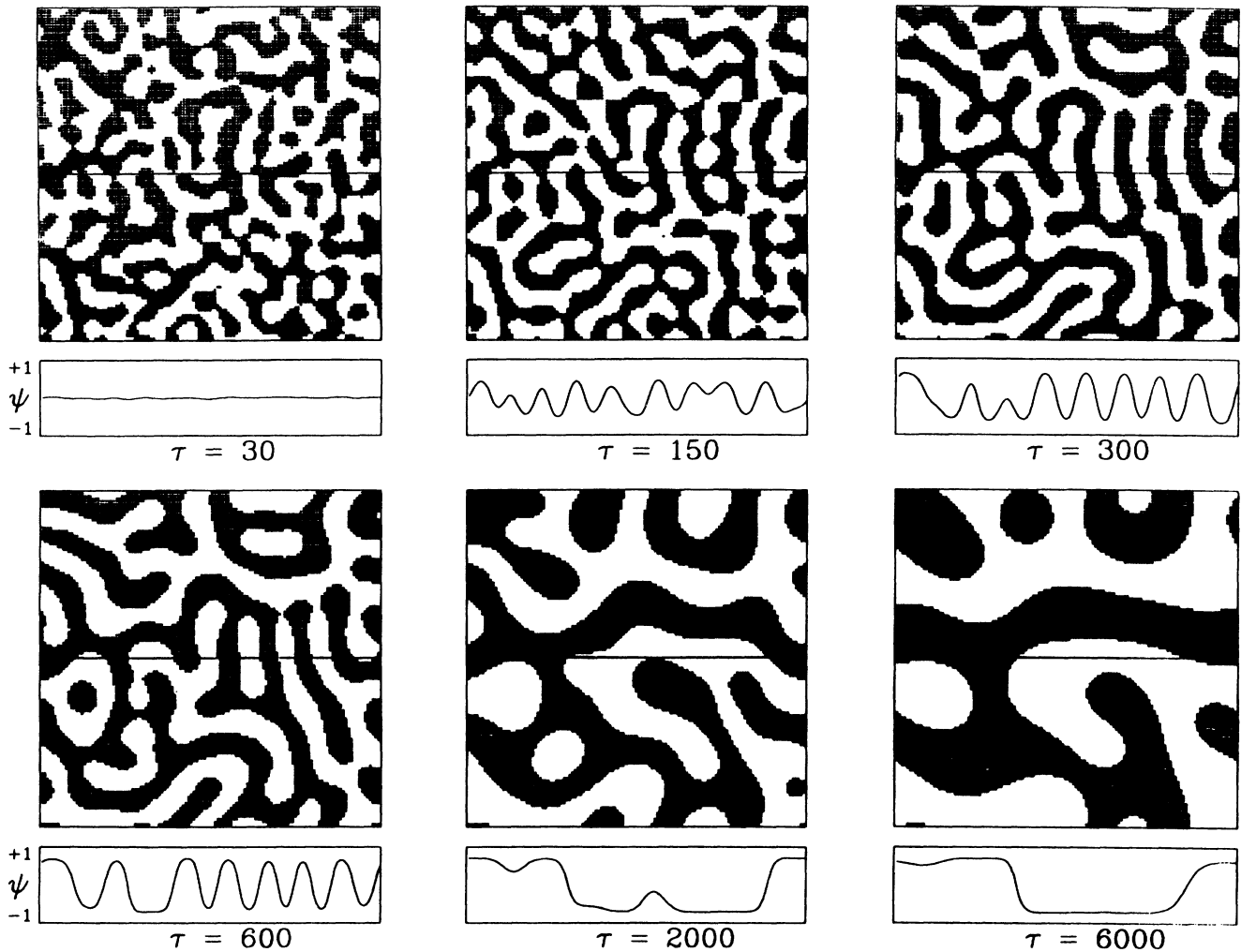


FIG. 6. Configuration pictures corresponding to  $MB_L$  for a critical quench in the thin film. (Run B:  $L = 0.1$ ,  $\beta = 5$ , and  $\psi_0 = 0$ .)

a given stripe for each of the stripes in the total pattern. During this stage,  $R_1(\tau)$  decreases to a minimum and then begins to rise. While the shape changes occur until quite a late time, the growth qualitatively sets in only beyond the minimum. The saturation of the domain size occurs earlier for an asymmetric mixture and in a thicker layer. For the thin layer, one needs to have

a larger system size in order to pursue the simulation to longer times.

$S(k, \tau)$  is illustrated in Fig. 9. Initially,  $S(k, \tau)$  is peaked about  $k_m$ . For the thick layer, beyond  $\tau = 1000$ , there is no significant inward shift of the peak position of the structure factor over the time regime considered; crossover effects are much smaller than those for the thin

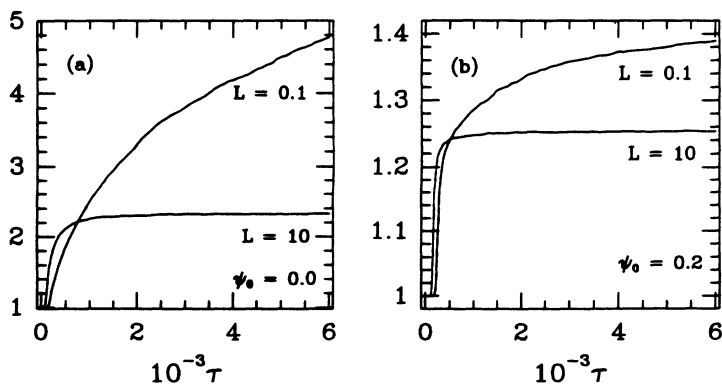


FIG. 7. (a) shows the inverse perimeter for  $MB_L$  in a critical quench and for the two film thicknesses and (b) shows the same for the off-critical quench.

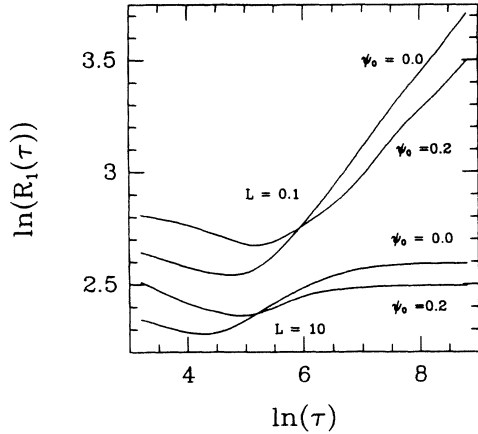


FIG. 8. Time dependence of  $\ln[R_1(\tau)]$  for  $MB_L$ .  $R_1(\tau)$  is proportional to the inverse of the first moment of the structure factor.

layer, where there is a considerable inward shift of the peak of  $S(k, \tau)$ .

At early times the system builds up a striplike pattern of period  $k_m$ , as is reflected in the initial peak of  $S(k, \tau)$ . After the contribution of this mode has saturated, the system dynamics is dominated by the *longer*-wavelength mode closest to  $k_m$ , which results in a thickening of the striplike pattern and a corresponding relaxation of the  $k_m$  mode. The system continues to coarsen towards smaller wave numbers until the dominant wavenumber becomes  $k_{eq}$ . This process leads to a thickening of the striplike pattern. This phenomena of mode saturation is a consequence of the nonlinearity. The rate of achieving this saturation is  $k$  dependent, with smaller  $k$  modes taking a longer time to saturate.

We have found [16] that the ordering state of the final configuration depends very much on the depth of the quench. Figure 10 shows that for deep quenches (low  $\beta$ ), the system gets trapped into a metastable disordered state, but for shallow quenches (high  $\beta$ ) the system continues to evolve towards the smectic ground state (in the absence of noise). Although these pictures correspond to  $MA_L$ , similar patterns for those parameters are obtained for  $MB_L$ . For the case of high  $\beta$ , the configuration of the quenched system during the late stage consists of large

domains, each one composed of several parallel stripes whose orientation defines the orientation of the domain. These different oriented domains can be characterized by an orientational order parameter. The system does not display scaling in the two-point correlation function of the scalar order parameter. However, one can expect scaling in the ordered-domain–ordered-domain correlation function or, equivalently, in the orientational order parameter correlation function. Elder, Viñals, and Grant [27] have studied the process of pattern formation in the two-dimensional Swift-Hohenberg equation and they have found dynamical scaling for the collective ordering of convective rolls. The scaling relationship they have found is of the form

$$S(k, \tau) = \tau^x f(|k - k_{eq}| \tau^x), \quad (29)$$

where  $x$  is a dynamical exponent related to the curvature of the rolls (they get  $x = 1/4$  for the nematic phase and  $x = 1/5$  for the smectic phase). This equation describes the correlation between these domains and is valid for large systems comprised of many domains. We expect this relationship to hold for our system at high  $\beta$  [16].

We now compare our simulation results with those of the early time theory described in the Appendix. Figure 11 compares the time evolution of the order-parameter contours taken from an arbitrary cut through a configuration generated by the simulation of a system of size  $128 \times 128$  (run *B*) and the theoretical time evolution obtained from using Eq. (25). Both correspond to the same initial random configuration. There are no significant deviations between the simulation and the early-time theory for  $\tau \leq 200$ , for systems in run *B* (thin layer) and for  $\tau \leq 125$  for systems in run *A* (thick layer). A similar comparison [28] for  $\beta = 0$  (i.e., in the absence of the LRRI) gives such quantitative agreement only up to about  $\tau = 50$ . Small deviations then occur, with the growth rate being consistently overestimated by the early-time theory. This is not surprising considering the approximations made: Eq. (25) is obtained by taking the growth rate of all the modes to be that of the maximally unstable mode  $k_m$ , which an overestimate for all other wave numbers. Also all the KYG-like solutions result from a theory with a single length scale. One is therefore unable to correctly generate the finite interface width or any intermediate time coarsening phenomena.

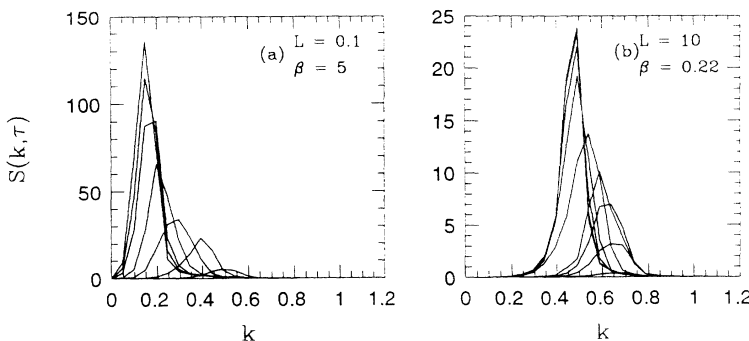


FIG. 9. Circularly averaged structure factor for  $MB_L$  and a critical quench. (a) corresponds to the thin film and the different curves correspond to  $\tau = 150, 420, 1000, 2000, 4000, 5000,$  and  $6000$  from right to left. (b) corresponds to the thick film and the different curves are for  $\tau = 60, 90, 120, 150, 420, 1000, 2000, 4000,$  and  $6000$  from right to left and bottom to top.

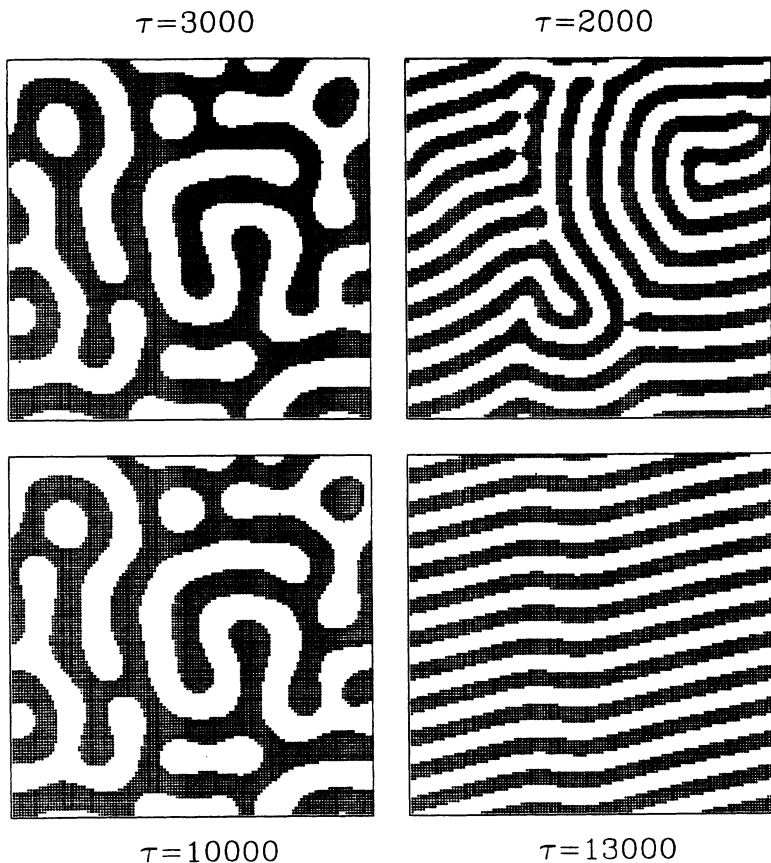


FIG. 10. Stripe patterns for  $MA_L$  showing the dependence of the final state on the strength of the dipolar interaction. The configurations correspond to  $L = 10, h = 0$ . The left pictures are for  $\beta = 0.10$  and the right ones for  $\beta = 0.34$ .

We find that in a relatively short time, the errors between the simulation and the linear theory diverge exponentially, while the errors between the simulation and Eq. (25) remain relatively constant. It seems, therefore, that this solution provides an excellent description of the early-time dynamics of a system with a scalar conserved

order parameter and with a long-range repulsive interaction.

The current outstanding theoretical problem with regard to the results described above is the construction of a better approximation of field-theoretic equations such as Eq. (A1) which would incorporate the coarsening ef-

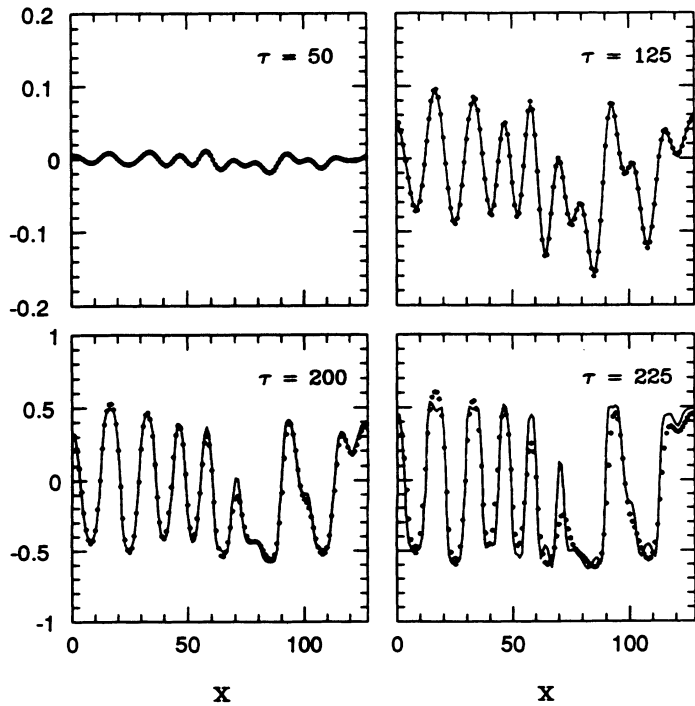


FIG. 11. Comparison between the KYG theoretical prediction (solid line) and simulation (points) for  $MB_L$  with  $L = 0.1, \beta = 5$ , and  $\psi_0 = 0$  (run B).

fects. This problem is also intimately related to the understanding of interface dynamics at intermediate and late stages of domain growth in systems with a conserved order parameter and in systems with a LRRI.

### C. Quenches into the hexagonal phase

We have also studied quenches from the uniform phase into the hexagonal phase. For  $MB_L$  we have essentially used an off criticality  $\psi_0 = 0.2$  ( $L = 10, \beta = 0.22$  and  $L = 0.1, \beta = 5.0$ ), and for  $MA_L$  we have used a field of  $h = 0.33$ , which in equilibrium produces an average magnetization  $\bar{m} = 0.23$  ( $L = 10, \beta = 0.22$ ). Since we are interested in deep quenches into the crystalline phase we expect the thermal noise to be irrelevant as long as it is not strong enough to put the system above the Kosterlitz-Thouless melting temperature. We tried three runs in to check this, and then we set  $\epsilon = 0$  for the rest of the runs.

Figures 12 and 13 show two evolving configurations for  $MB_L$  systems belonging to runs  $C$  and  $D$  (thick and thin

layers, respectively). Here positive deviations from the system's average value of  $\psi$  (i.e.,  $\psi > \psi_0$ ) are shaded dark. In contrast to the percolating domain structure obtained from quenches into the stripe phase, the configuration consists of a sea of droplets. At early times, the morphology looks nearly interconnected (bicontinuous); but soon the unshaded threads develop bulges and necks and necks pinch away to create elongated clusters which evolve towards the circular shape. The initial stage dynamics is once again accompanied by both the shape changes and domain growth.

Figure 14 shows the circularly averaged structure factor for  $MB_L$ . Even though the underlying morphology is dramatically different, the structure factors in Figs. 14 and 9 look very similar. For the thick layer, both the peak position and peak height are quantitatively close in the two cases of  $\psi_0 = 0$  and 0.2. For the thin layer, the coarsening is slower for the off-critical quench. Because of nearly quantitative similarity of structure factors, the morphology differences between the two phases are better characterized by studying topological features of the two phases. An example is the cluster-size distribution which

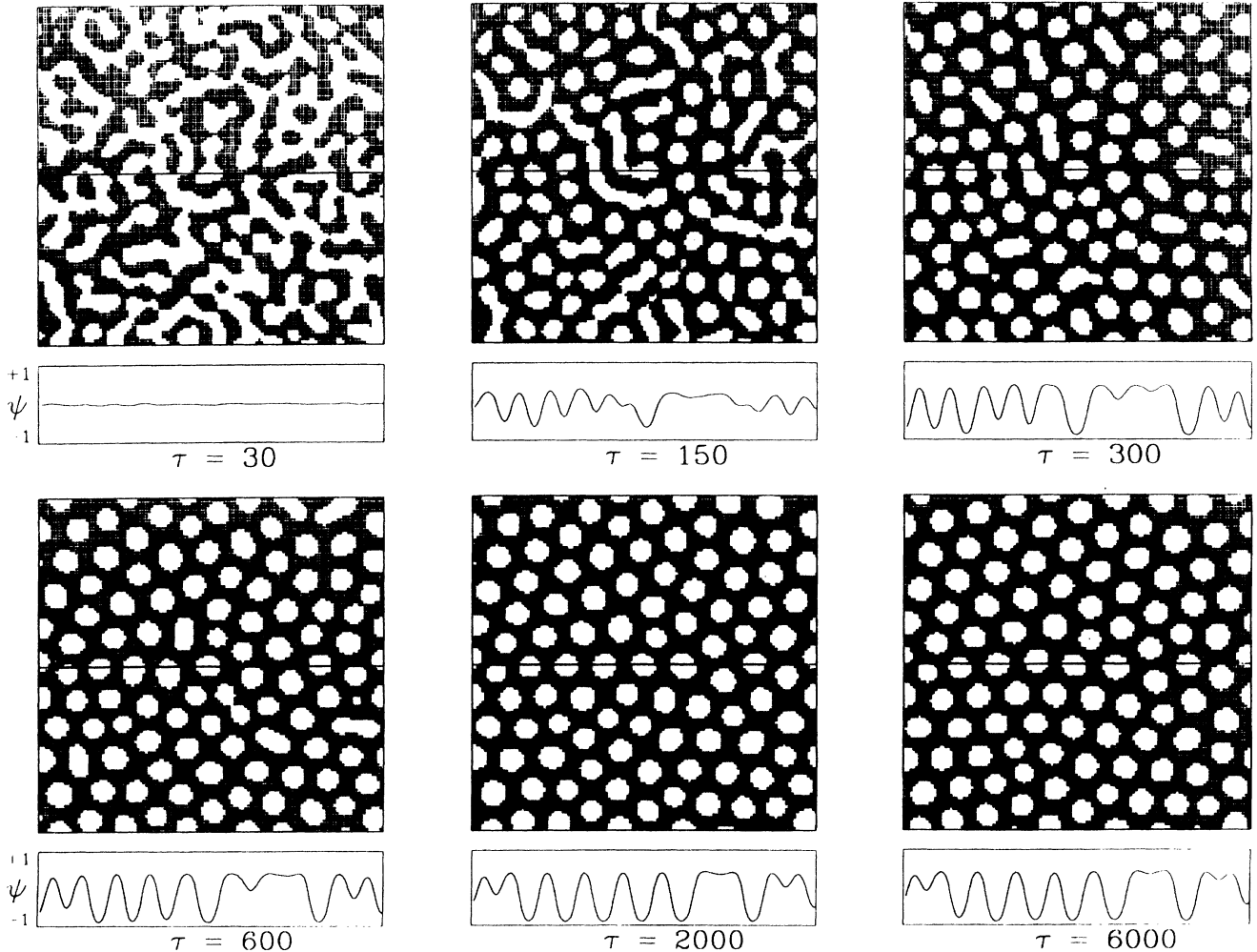


FIG. 12. Configuration pictures corresponding to  $MB_L$  for an off-critical quench in the thick film. (Run  $C$ :  $L = 10, \beta = 0.22$ , and  $\psi_0 = 0.2$ .)

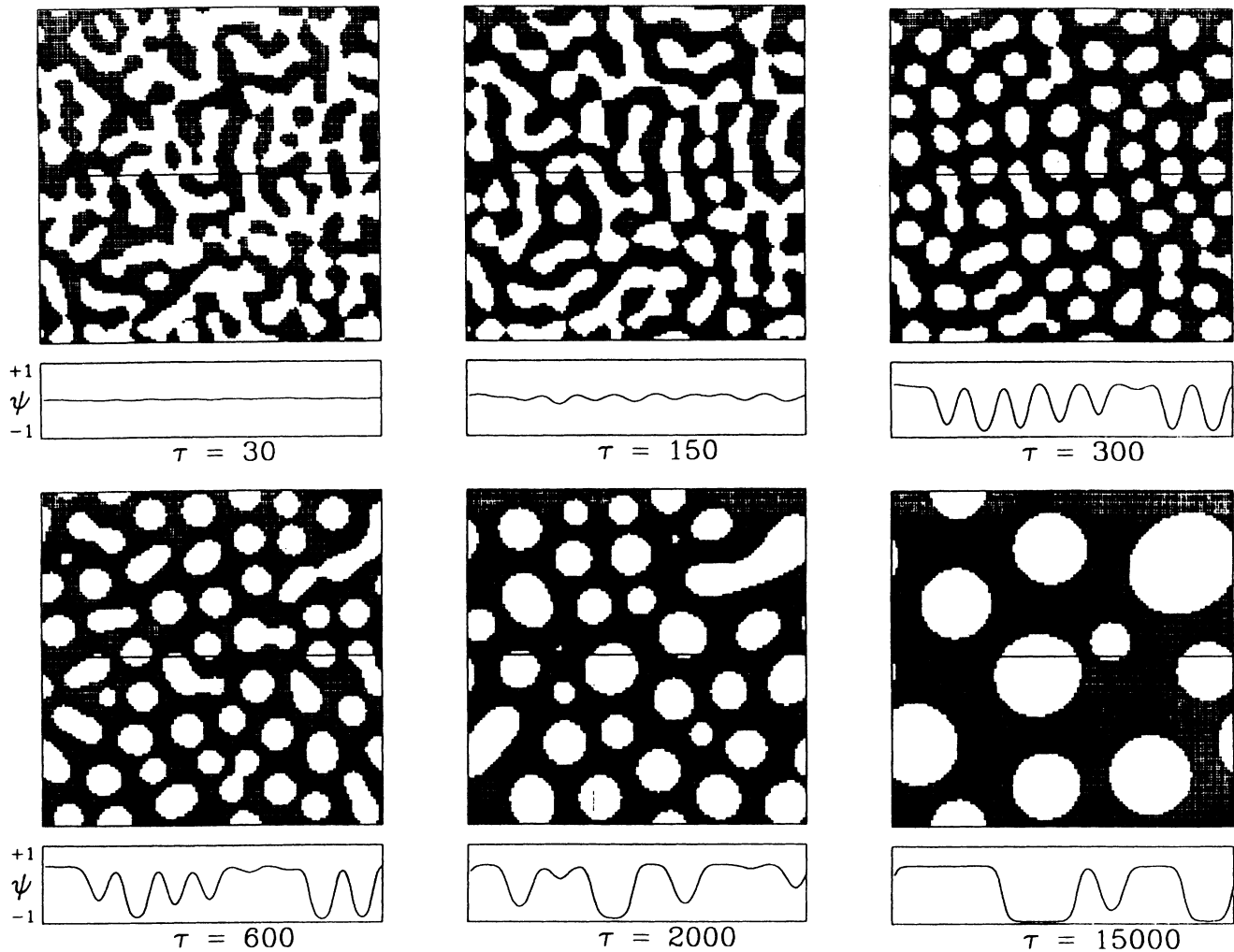


FIG. 13. Configuration pictures corresponding to  $MB_L$  for an off-critical quench in the thin film. (Run  $D$ :  $L = 0.1$ ,  $\beta = 5$ , and  $\psi_0 = 0.2$ .)

is straightforward to define only for the asymmetric case.

A radius of gyration was used to define the cluster radius

$$R_c = \left[ \frac{2}{l^2} \sum_i (\mathbf{r}_i - \mathbf{r}_{cm})^2 \right]^{\frac{1}{2}}. \quad (30)$$

The sum is over the  $l^2$  lattice sites of the cluster.  $\mathbf{r}_i$  is the position of lattice site  $i$  and  $\mathbf{r}_{cm}$  is the position of the cluster's center. (The factor of 2 ensures that  $R_c$  reduces to the usual cluster radius for circular clusters.) In Fig. 15 (bottom) the arithmetic average of the radii of gyration of all the clusters at a given time  $\langle R_c \rangle$  is plotted as a function of time  $\tau$  for runs  $C$  and  $D$  and for  $MA_L$ . For the sake of comparison, we have also included the curve

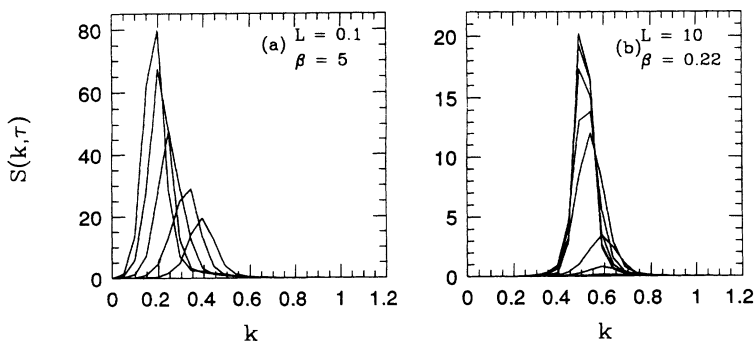


FIG. 14. Circularly averaged structure factor for  $MB_L$  and an off-criticality of  $\psi_0 = 0.2$ . (a) corresponds to the thin film and the different curves correspond to  $\tau = 420$ , 1000, 2000, 4000, and 6000 from right to left. (b) corresponds to the thick film and the different curves are for  $\tau = 90$ , 120, 150, 420, 1000, 2000, 4000, and 6000 from right to left and bottom to top.

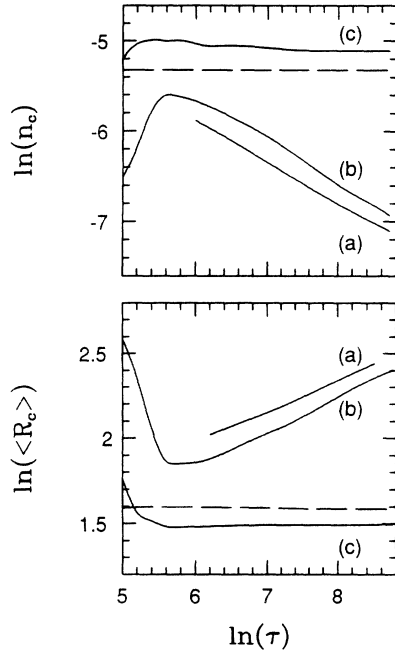


FIG. 15. The top figure shows the time dependence of the cluster density  $n_c$  and the bottom figure shows the time dependence of the arithmetic average of the radii of gyration  $\langle R_c \rangle$  of all the clusters. The solid lines correspond to  $MB_L$  with  $\psi_0 = 0.2$  and the dashed lines correspond to  $MA_L$  with  $h = 0.33$ . (a)  $\beta = 0$  (model B). (b)  $\beta = 5$ ,  $L = 0.1$ . (c)  $\beta = 0.22$ ,  $L = 10$ .

for model B ( $\beta = 0$ ) taken from Ref. [25]. Since  $MA_L$  has reached its  $k_{eq}$ ,  $\ln(\langle R_c \rangle)$  is constant. We can see that  $MB_L$  tends to a saturation value (in contrast to model B). Run C achieves it quite fast while the clusters of the system in run D are still growing over the time regime considered. Figure 15 (top) shows the time dependence of the cluster density  $n_c$ ;  $n_c$  is defined as the number of clusters per unit area in the system. Once again, for comparison, we have included the case of model B [25]. Again, the curve is a constant for  $MA_L$ . For  $MB_L$ , a comparison of Fig. 8 and the two panels of Fig. 15 shows that  $R_1(\tau)$  and  $\langle R_c(\tau) \rangle$  reach their minimum approximately

at the same time when  $n_c$  reaches its maximum. This corresponds to the time when the system has evolved to a morphology made up of isolated clusters, and these clusters have on average the smallest size throughout the time evolution while their total number is the largest. (The same also happens for  $MA_L$ , except that at much earlier times.)

We have also computed the time dependence of the cluster distribution function  $f(R, \tau)$ . Here  $f$  is defined such that  $f(R, \tau)dR$  is the probability of finding a cluster with radius between  $R$  and  $R+dR$  and it satisfies the normalization  $\int f(R, \tau)dR = 1$ . In Fig. 16 we have plotted  $f(R/\langle R_c \rangle)$ . As time increases and clusters become more circular, the distribution function moves steadily towards larger values of  $\frac{R}{\langle R_c \rangle}$ , until it centers around  $\frac{R}{\langle R_c \rangle} = 1$  for  $\tau \geq 1000$  and  $\tau \geq 100$  for  $MB_L$  and  $MA_L$ , respectively.

To take a closer look at the local geometrical properties of the system, we have also computed the angular distribution of nearest neighbors (Fig. 17) for the latest configuration ( $\tau = 6000$ ) in Fig. 12. Beginning roughly with  $\tau = 150$ , the morphology shows that the configuration is made up of clusters with a closed surface and the interconnected morphology of earlier times is no longer present. Thus it is straightforward to identify various clusters. For each cluster with a closed surface in the system (most of these clusters are nearly circular at late times), we determine its center of mass. Next we use Voronoi constructions to determine the positions of the cluster's nearest neighbors and choose a reference direction midway between the pair of nearest neighbors which are closest to one another. (For different clusters, this reference axis will in general point in different directions.) We denote by  $n(\theta)\Delta\theta$  the number of clusters that have one of their first nearest neighbors lying between  $\theta$  and  $\theta + \Delta\theta$ . Anticipating an approximately hexagonal geometry that is visually clear in the picture, we use  $\Delta\theta = 30^\circ$ . Figure 17(a) shows the histogram  $n(\theta)$ ; for a perfect local hexagonal morphology, all the minima of this distribution function would be zero and the peaks would occur with  $n(\theta) = 1/6$  (we have actually seen this in a  $128^2$  rectangular system for  $MA_L$  that has reached the crystalline ground state at  $\tau = 20000$ ). Figure 17(b) shows the distribution of coordination number  $z$ , i.e., the number of clusters that have  $z$  nearest neighbors. Figure 17 shows quantitatively that the morphology is *locally* hexagonal.

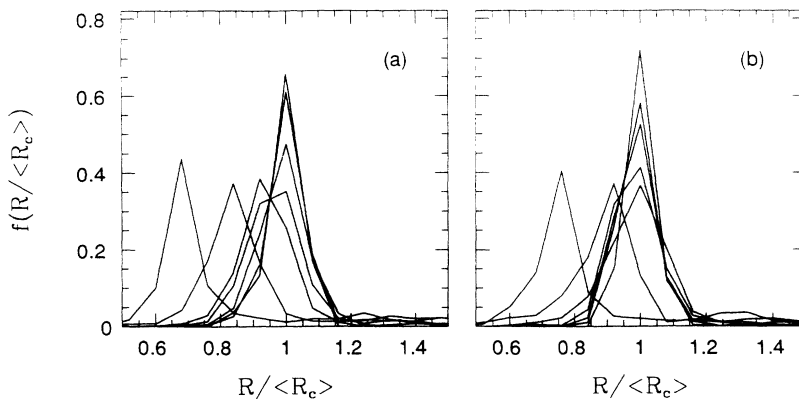


FIG. 16. Cluster distribution function. (a)  $MB_L$  for  $\tau = 150, 180, 300, 600, 1500, 5000$ , and  $6000$  from left to right and bottom to top. (b)  $MA_L$  for  $\tau = 60, 70, 100, 200, 500, 1000$ , and  $4000$  from left to right and bottom to top.

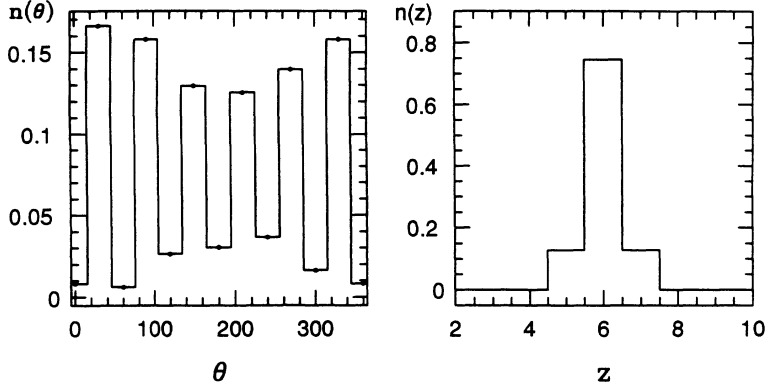


FIG. 17. Angular distribution of nearest neighbors (left) and distribution of coordination number (right) for  $MB_L$ , corresponding to the last configuration of Fig. 12 ( $\tau = 6000$ ).

While Fig. 17 refers to the geometrical properties of the local lattice, Fig. 18 shows the properties of a single cluster. It illustrates how the average shape of a cluster approaches a circle as time increases. Let  $r_i(\vartheta)$  denote the distance of the cluster surface from its center of mass, as a function of the angle  $\vartheta$ , and  $\bar{R}_i$  the mean radius. Then the difference  $f_i(\vartheta) = r_i(\vartheta) - \bar{R}_i$  will be zero for a perfectly circular cluster and the function  $f_i(\vartheta)$  will, for a noncircular cluster, have both positive and negative values. For convenience, the direction of maximum elongation is chosen as the reference direction  $\vartheta = 0$ . In terms of such a local reference direction, we define a quantity  $m(\vartheta)$ ,

$$m(\vartheta) = \frac{1}{N_B} \sum_i \int_{\vartheta}^{\vartheta+\Delta\vartheta} f_i(\vartheta) d\vartheta, \quad (31)$$

where  $\Delta\vartheta$  is a small angle (a value of  $10^\circ$  is used),  $N_B$  is the total number of clusters, and the sum runs over all clusters. In Fig. 18 we show  $m(\vartheta)$  for  $MB_L$  for  $\tau = 420$  and  $\tau = 6000$  (the last configuration in Fig. 12). Statistically the cluster shape is approaching a circular shape in time.  $MA_L$  shows similar behavior.

Finally in Fig. 19 we show two more related quantities which also depict the approach to the circular shape. The first quantity depicted in Fig. 19(a) is the angular integral,

$$M = \frac{1}{N_B} \sum_i \int_0^{2\pi} |f_i(\vartheta)| d\vartheta. \quad (32)$$

A collection of perfect circular clusters has  $M = 0$ . Thus we would expect  $M \rightarrow 0$  for  $\tau \rightarrow \infty$ . In the semi-logarithmic plot of  $M(\tau)$ , the qualitative features of the curves for  $MA_L$  and  $MB_L$  are similar. There is a linear region, roughly between  $\tau = 150$  and  $\tau = 300$  for  $MB_L$  and between  $\tau = 50$  and  $\tau = 100$  for  $MA_L$ , that corresponds to the time span when separated closed clusters are established but their shapes are rapidly changing to elliptic ones. In this region  $M \sim \tau^{-\omega_i}$ , with  $\omega_B \sim 1.74$  and  $\omega_A \sim 1.19$ . The beginning of the second linear region roughly coincides with the minima in  $\langle R_c \rangle$  and in  $R_1(\tau)$  (or alternatively, the maxima in  $n_c$ ). This is the time when the system has evolved to a morphology made up of nearly elliptical clusters. Subsequent to this point, this second region shows that the pace of reaching the equilibrium circular shape is slowed down as compared to that in the first region. Here again  $M$  varies as a power law  $M \sim \tau^{-\Omega_i}$ , with  $\Omega_B \sim 0.34$  and  $\Omega_A \sim 0.14$ .

To further quantify the symmetry of the individual clusters, we have expanded the function  $f(\vartheta)$  in circular harmonics as

$$f(\vartheta) = \sum_{n=1}^{\infty} [a_n \cos(n\vartheta) + b_n \sin(n\vartheta)]. \quad (33)$$

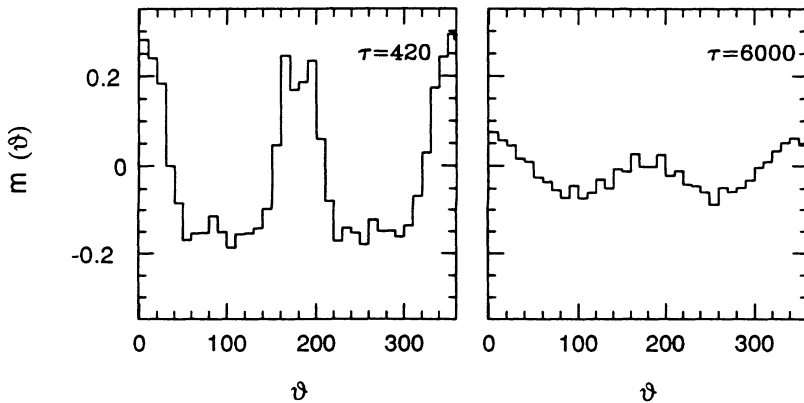


FIG. 18. Average angular deviation from the circular shape for clusters belonging to run  $C$ .

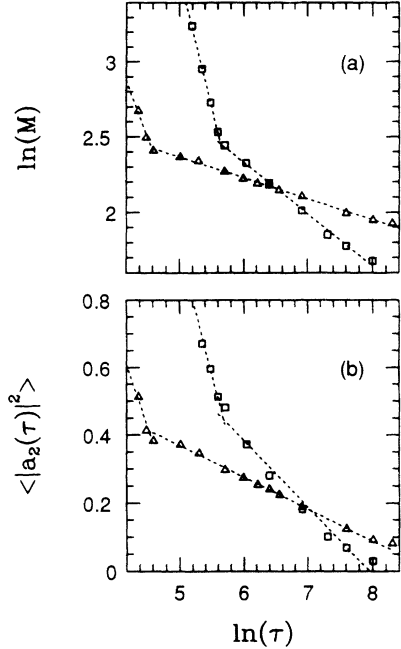


FIG. 19.  $\ln(M)$  and  $\langle |a_2(\tau)|^2 \rangle$  vs  $\ln(\tau)$  indicating a twofold symmetry decaying towards a circular symmetry. The triangles correspond to  $MA_L$  and the squares to  $MB_L$  (run  $C$ ). The dotted lines are linear fits.

We have computed the coefficients for  $n = 1, 2, 3, \dots, 12$  and found that the coefficients  $a_n$  are  $\sim 10^{-2}$  or  $10^{-3}$  and are larger by one or two orders of magnitude than the coefficients  $b_n$ . All the coefficients, except  $a_2$ , decay very little at early times and remain essentially constant throughout the time span considered.  $a_2$ , on the other hand, is larger than the rest of the coefficients,  $a_2 \sim 10^{-1}$ , and has a sharp decay in early and intermediate times. Figure 19(b) shows  $\langle |a_2(\tau)|^2 \rangle$ , indicating a twofold symmetry decaying towards a circular symmetry.  $f(\vartheta)$  and  $M$  give a quantitative idea of how the shaping process of disks occurs after a quench from a disordered state. From the pictures shown, it can be seen that higher harmonic fluctuations do not play an important role in the shaping of clusters, at least for intermediate and late times. One can therefore expect that for our system only the elliptical instability is important, as has been stated theoretically [4]. In summary we conclude that apart from time scales, the processes of the emergence and shaping of individual clusters are very similar for  $MA_L$  and  $MB_L$ . There are also strong similarities in the crystalline ordering processes [15], more details of this will be given in a subsequent paper.

## VI. CONCLUSIONS

In this paper, we have studied the dynamics of quenched quasi-two-dimensional systems with a scalar order parameter and competing interactions. We have considered systems with both conserved ( $MB_L$ ) and non-

conserved ( $MA_L$ ) order parameters and with a long-range repulsive interaction. In both systems, there is a competition between the short-range attractive forces, which favor dipolar alignment and the long-range repulsive interactions, which favor dipolar antialignment. This leads to the formation of modulated phases with either lamellar or hexagonal symmetry. We have presented a  $T = 0$  phase diagram for a particular thickness of the film and discussed the dependence of these phases on the parameters of the system.

The dynamics of these systems are very rich. In this paper we have studied the initial stages of the evolution that correspond to the processes of domain emergence and shaping that take place following the quench. In the early-time regime, the instability amplifies the fluctuations present in the initial conditions, saturates them, and forms sharp interfaces. This time regime is dominated by  $k_m$ , the maximally unstable wave number of the linear dispersion relation. During this time, the amplitude of the order parameter grows towards its saturation value. This regime is well explained through an approximate solution based on an extension of the KYG theory of the appropriate Langevin equation. We have applied this KYG extension to  $MB_L$  and found that this solution accounts for some of the nonlinearities present in the model. It yields a nonexponential growth rate of the order parameter. There are no significant differences between the KYG solution and simulation results at early times. In contrast, the intermediate-time regime is dominated by the wave number of the equilibrium modulated structure  $k_{eq}$  ( $k_{eq} < k_m$ ). The characteristic time of this regime is the time that the domains require to reach their equilibrium wavelength. Thus the dynamics presented in this paper display crossover phenomena, as the characteristic wave number of the system changes from  $k_m$  to  $k_{eq}$ . These crossover phenomena are not described by the KYG solution. However, the agreement between the simulation of  $MB_L$  and the KYG solution (up to  $\tau \sim 200$ ) is much better than that for the simulations of model B (up to  $\tau \sim 30$ ) [28].

Immediately after the quench, the system acquires a very complicated morphology of irregular interpenetrating domains that percolate through the system. As time evolves these domains become more regular as they evolve towards their stripe or disk shape. Eventually, there comes the stage (sooner for thicker films and for higher dipolar strengths) where the curve of the characteristic wavelength versus time becomes approximately flat after which the number of domains stays almost constant and the distribution function of the widths of the stripes or the radii of the disks becomes highly peaked on the equilibrium value. At this point the system is a disordered liquid of monodisperse stripes or disks, without global orientational order but with local orientational order. Further evolution of the system towards the crystalline order (expected for zero-temperature ground state) becomes slow and hampered by the presence of defects. There are several nonvanishing length scales: the interface thickness, the domain size, and the distance between domain centers. The two-point correlation function of the scalar order parameter does not

present scaling. However, one can see in the configuration pictures the formation of macrodomains (comprised of many stripes or disks) characterized by a certain orientation. The evolution of these macrodomains, as the system evolves from this disordered liquid towards its ground state gaining orientational and positional order, will be the subject of our forthcoming paper [16].

### ACKNOWLEDGMENT

This research was supported by the NSERC of Canada.

### APPENDIX

In this appendix, we apply the singular perturbation theory of Kawasaki, Yalabik, and Gunton to  $MB_L$ . Previously, this method has been applied to a variety of other dynamical systems [28,13]. The starting point is Eq. (18) with  $\epsilon = \psi_0 = 0$ :

$$\frac{\partial \psi_{\mathbf{k}}(\tau)}{\partial \tau} = \gamma_{\mathbf{k}} \psi_{\mathbf{k}}(\tau) - \frac{k^2}{2} \sum_{\mathbf{k}'} \sum_{\mathbf{k}''} \psi_{\mathbf{k}'}(\tau) \psi_{\mathbf{k}''}(\tau) \psi_{\mathbf{k}-\mathbf{k}'-\mathbf{k}''}(\tau), \quad (\text{A1})$$

with a linear dispersion relation

$$\gamma_{\mathbf{k}} = \frac{k^2}{2} [1 - k^2 - \beta g(k)]. \quad (\text{A2})$$

In analogy to KYG, we devise an infinite-order singular perturbation theory around the linear solution

$$\psi_{\mathbf{k}}^0(\tau) = e^{\gamma_{\mathbf{k}} \tau} \psi_{\mathbf{k}}(\tau = 0). \quad (\text{A3})$$

Formal integration of the integral form of Eq. (A1) leads to

$$\begin{aligned} \psi_{\mathbf{k}}(\tau) &= \psi_{\mathbf{k}}^0(\tau) - \frac{k^2}{2} \int_0^\tau d\tau' e^{\gamma_{\mathbf{k}}(\tau-\tau')} \\ &\times \sum_{\mathbf{k}'} \sum_{\mathbf{k}''} \psi_{\mathbf{k}'}(\tau') \psi_{\mathbf{k}''}(\tau') \psi_{\mathbf{k}-\mathbf{k}'-\mathbf{k}''}(\tau') \\ &= \sum_{n=0}^{\infty} (2n-1)!! D_n, \end{aligned} \quad (\text{A4})$$

where

$$D_n = \left(-\frac{1}{2}\right)^n e^{\gamma_{\mathbf{k}} \tau} \sum_{\mathbf{k}_1} \sum_{\mathbf{k}_2} \dots \sum_{\mathbf{k}_{2n+1}} \delta\left(\mathbf{k} - \sum_{i=1}^{2n+1} \mathbf{k}_i\right) \left(\prod_{i=1}^{2n+1} \psi_{\mathbf{k}_i}(\tau = 0)\right) \left(\prod_{a=0}^{n-1} \left|\sum_{i=2a+1}^{2n+1} \mathbf{k}_i\right|^2\right) f_n(\{x_n\}; \tau), \quad (\text{A5})$$

with

$$\begin{aligned} f_n(\{x_n\}; \tau) &= \int_0^\tau d\tau_1 \int_0^{\tau_1} d\tau_2 \dots \int_0^{\tau_{n-1}} d\tau_n \\ &\times \exp\left(\sum_{i=1}^n x_i \tau_i\right) \end{aligned} \quad (\text{A6})$$

and

$$\begin{aligned} x_i &= \gamma(k_{2i-1}) + \gamma(k_{2i}) \\ &+ \gamma\left(\left|\sum_{j=2i-1}^{2n+1} \mathbf{k}_j\right|\right) - \gamma\left(\left|\sum_{j=2i-1}^{2n+1} \mathbf{k}_j\right|\right). \end{aligned} \quad (\text{A7})$$

In the infinite series Eq. (A4), each term grows exponentially faster in time than the preceding term. So in any approximation, it is essential to resume the infinite series, keeping all the terms. The  $n$ th order term can be approximated using approximations analogous to those in Ref. [24]. *First*, in evaluating the time integrals in Eq. (A6) using Laplace transforms, only the most dominant pole is counted since this gives an exponentially larger contribution than the rest which may safely be neglected. This introduces an error of order

$$\left(\frac{\tau}{2 \ln 16}\right)^2 k_{\text{cutoff}}^4 e^{(-2\gamma_m \tau)}. \quad (\text{A8})$$

*Second*, assume that the dominant contribution to the wavevector sums occurs when  $k_i \approx k_m$ , the maximally unstable mode. *Third*, assume also that the directions of each of the  $\mathbf{k}_i$  which is summed is distributed isotropically. This is to a large extent an uncontrolled approximation. As a result, the KYG-type solutions are unable to describe coarsening, i.e., the shift in the position of  $k_m$  with time, as is important for models with conserved order parameter. For our long-range interaction, the inability of the KYG-type solution to incorporate a shift in  $k_m$  restricts its validity as a description of the system's dynamics to the early-time regime. During this regime, the dynamics of the system is dominated by  $k_m$ . However, at equilibrium the system is characterized by domain widths with the equilibrium wave vector  $k_{\text{eq}}$ . Therefore the crossover that takes place as the modulation length changes from  $\lambda = 2\pi/k_m$  to  $\lambda = 2\pi/k_{\text{eq}}$  is not incorporated in the approximate solution. It is, however, an improvement over the linear solution at early times.

Straightforward algebra gives the  $n$ th-order term as

$$D_n \approx \frac{\Gamma(\alpha_k)}{\Gamma(n + \alpha_k)} \left( \frac{-k^2}{4\gamma_m} \right)^n \sum_{\mathbf{x}} e^{i\mathbf{k}\cdot\mathbf{x}} [\psi^0(\mathbf{x}, \tau)]^{2n+1}, \quad (\text{A9})$$

where

$$\alpha_k = \frac{3\gamma_m - \gamma_k}{2\gamma_m}, \quad (\text{A10})$$

where  $\Gamma$  is the gamma function and  $\psi^0(\mathbf{x}, \tau)$  is the inverse Fourier transform of  $\psi_{\mathbf{k}}^0(\tau)$ . Substitution of this result into Eq. (A5) gives a closed form result

$$\psi_{\mathbf{k}}(\tau) = \sum_{\mathbf{x}} e^{i\mathbf{k}\cdot\mathbf{x}} \psi^0(\mathbf{x}, \tau) F\left(\frac{1}{2}, 1; \alpha_k; -z\right), \quad (\text{A11})$$

with

$$z = \frac{k^2 [\psi^0(\mathbf{x}, \tau)]^2}{2\gamma_m}, \quad (\text{A12})$$

where  $F$  is the hypergeometric function.

For numerical evaluation it is convenient to rewrite Eq. (A11) in the following manner:

$$\psi_{\mathbf{k}}(\tau) = \sum_{\mathbf{x}} e^{i\mathbf{k}\cdot\mathbf{x}} \psi^0(\mathbf{x}, \tau) \frac{(\alpha_k - 1)}{\sqrt{1+z}} \left( \frac{1+z}{z} \right)^{\alpha_k - 1} \times B_{\frac{z}{1+z}}\left(\frac{1}{2}, \alpha_k - 1\right), \quad (\text{A13})$$

where  $B_x(a, b)$  is the incomplete beta function.

- 
- [1] Reviews are given by K. Binder, *Physica* (Amsterdam) **140A**, 35 (1986); J.D. Gunton, M. San Miguel, and P.S. Sahni, in *Phase Transitions and Critical Phenomena*, edited by C. Domb and J.L. Lebowitz (Academic, London, 1983), Vol. 8, and references therein.
- [2] S.M. Allen and J.W. Cahn, *Acta Metall.* **27**, 1085 (1979).
- [3] I.M. Lifshitz and V.V. Slyozov, *J. Phys. Chem. Solids* **19**, 35 (1961).
- [4] C. Kooy and U.ENZ, *Phillips Res. Rep.* **15**, 729 (1960); A.A. Thiele, *J. Appl. Phys.* **41**, 1139 (1970); Bell Lab. Tech. J. **48**, 3287 (1969); W.F. Druyvesteyn and J.W. Dorleijn, *Phillips Res. Rep.* **26** 11 (1971); J.A. Cape and G.W. Lehman, *J. Appl. Phys.* **42**, 5732 (1971); J.A. Cape, *ibid.* **43**, 3551 (1972); T. Garel and S. Doniach, *Phys. Rev. B* **26**, 325 (1982).
- [5] Y. Yafet and E.M. Gyorgy, *Phys. Rev. B* **38**, 9145 (1988)
- [6] A.O. Tsebers and M.M. Maiorov, *Magnetohydrodynamics* **16**, 21 (1980); A. O. Tsebers, *ibid.* **17**, 113 (1981); R.E. Rosensweig, M. Zahn and R. Shumovich, *J. Magn. Magn. Mat.* **39**, 127 (1983); S. A. Langer, R.E. Goldstein, and D.P. Jackson (unpublished).
- [7] T. Mitsui and J. Furuichi, *Phys. Rev.* **90**, 193 (1953).
- [8] Reviews are given by C.M. Knobler and R.C. Desai, *Annu. Rev. Phys. Chem.* **43**, 207 (1992); H.M. McConnell, *ibid.* **42**, 171 (1991); H. Möhwald, *ibid.* **41**, 441 (1990).
- [9] See, for example: P. de Gennes, *The Physics of Liquid Crystals* (Clarendon Press, Oxford, 1974).
- [10] W.L. McMillan, *Phys. Rev. B* **12**, 1187 (1975).
- [11] J.R. Thomsen, W. Cowan, M.J. Zuckermann, and M. Grant, in *Proceedings of the XVIII Winter Meeting On Statistical Physics, Oaxatepo, Mexico, 1989*, edited by A.E. Gonzalez, C. Varea, and M. Medina-Noyola (World Scientific, Singapore, 1989).
- [12] L.Q. Chen and A.G. Khachatryan, *Phys. Rev. Lett.* **70**, 1477 (1993).
- [13] C. Roland and R.C. Desai, *Phys. Rev. B* **42**, 6658 (1990).
- [14] A brief description of some aspects of the dynamics of MB<sub>L</sub> is given by R.C. Desai, C. Sagui, and K.R. Elder, in *Structure and Dynamics of Strongly Interacting Colloids and Supramolecular Aggregates in Solution*, edited by S.H. Chen *et. al.* (Kluwer, Dordrecht, 1992), p. 205.
- [15] Celeste Sagui and Rashmi C. Desai, *Phys. Rev. Lett.* **71**, 3995 (1993).
- [16] Celeste Sagui and Rashmi C. Desai (unpublished).
- [17] M. Hurley and S. Singer, *J. Phys. Chem.* **96**, 1938 (1992); **96**, 1951 (1992); *Phys. Rev. B* **46**, 5783 (1992).
- [18] D. Andelman, F. Brochard, and J. F. Joanny, *J. Chem. Phys.* **86**, 3673 (1987).
- [19] We have introduced a cutoff by comparing the order-parameter profiles computed with  $s$  modes and with  $(s + 2)$  modes: when the difference between these is negligible, we assume that the series has effectively converged. On average, it means keeping around 16 modes.
- [20] P. Molho, J. Gouzerh, J.C.S. Levy, and J.L. Porteseil, *J. Magn. Magn. Mat.* **54-57**, 857 (1986).
- [21] H.M. McConnell, *J. Phys. Chem.* **94**, 4728 (1990); T.K. Vanderlick and H. Möhwald, *ibid.* **94**, 886 (1990).
- [22] M. Seul, *Physica A* **168**, 198 (1990); M. Seul and M.J. Sammon, *Phys. Rev. Lett.* **64**, 1903 (1990); M. Seul, L.R. Monar, L. O’Gorman, and R. Wolfe, *Science* **254**, 1616 (1991).
- [23] A.J. Dickstein, R.E. Goldstein, D.P. Jackson, S.A. Langer, and E. Shyamsunder (unpublished).
- [24] K. Kawasaki, M.C. Yalabik and J.D. Gunton, *Phys. Rev. A* **17**, 455 (1978).
- [25] T.M. Rogers, K.R. Elder, and R.C. Desai, *Phys. Rev. B* **37**, 9638 (1988), T.M. Rogers and R.C. Desai, *ibid.* **39**, 11 956 (1989).
- [26] W.H. Press, B.P. Flannery, S.A. Teukolsky, and W.T. Vetterling, *Numerical Recipes* (Cambridge University Press, Cambridge, 1986).
- [27] K. Elder, J. Viñals, and M. Grant, *Phys. Rev. Lett.* **68**, 3024 (1992).
- [28] See K. Elder, Ph.D. thesis, University of Toronto, 1989, for an analogous calculation as applied to model  $B$  systems.

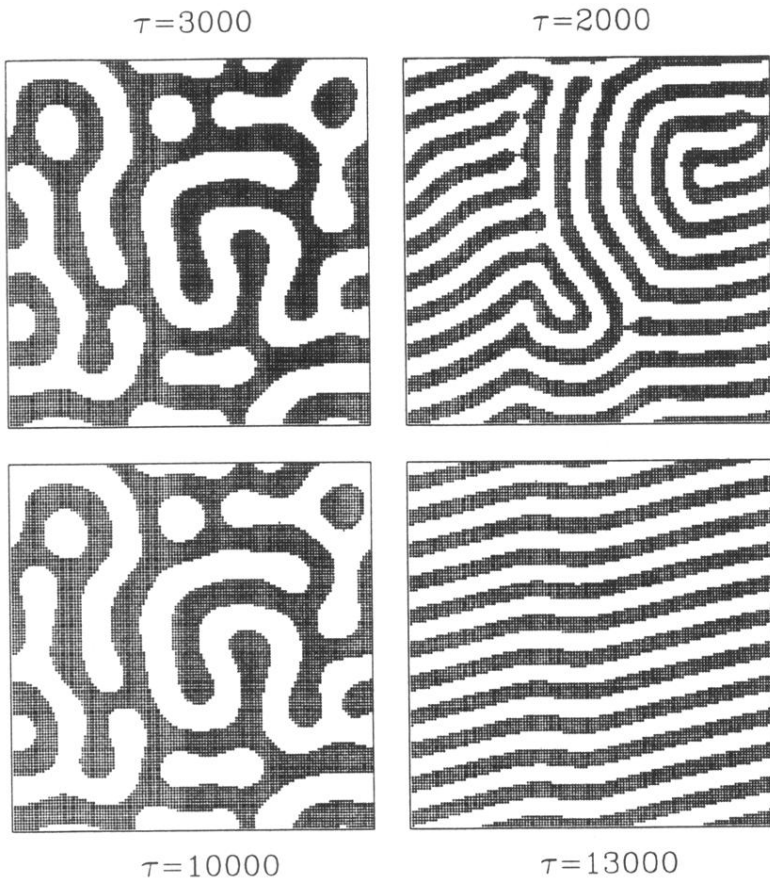


FIG. 10. Stripe patterns for  $MA_L$  showing the dependence of the final state on the strength of the dipolar interaction. The configurations correspond to  $L = 10$ ,  $h = 0$ . The left pictures are for  $\beta = 0.10$  and the right ones for  $\beta = 0.34$ .

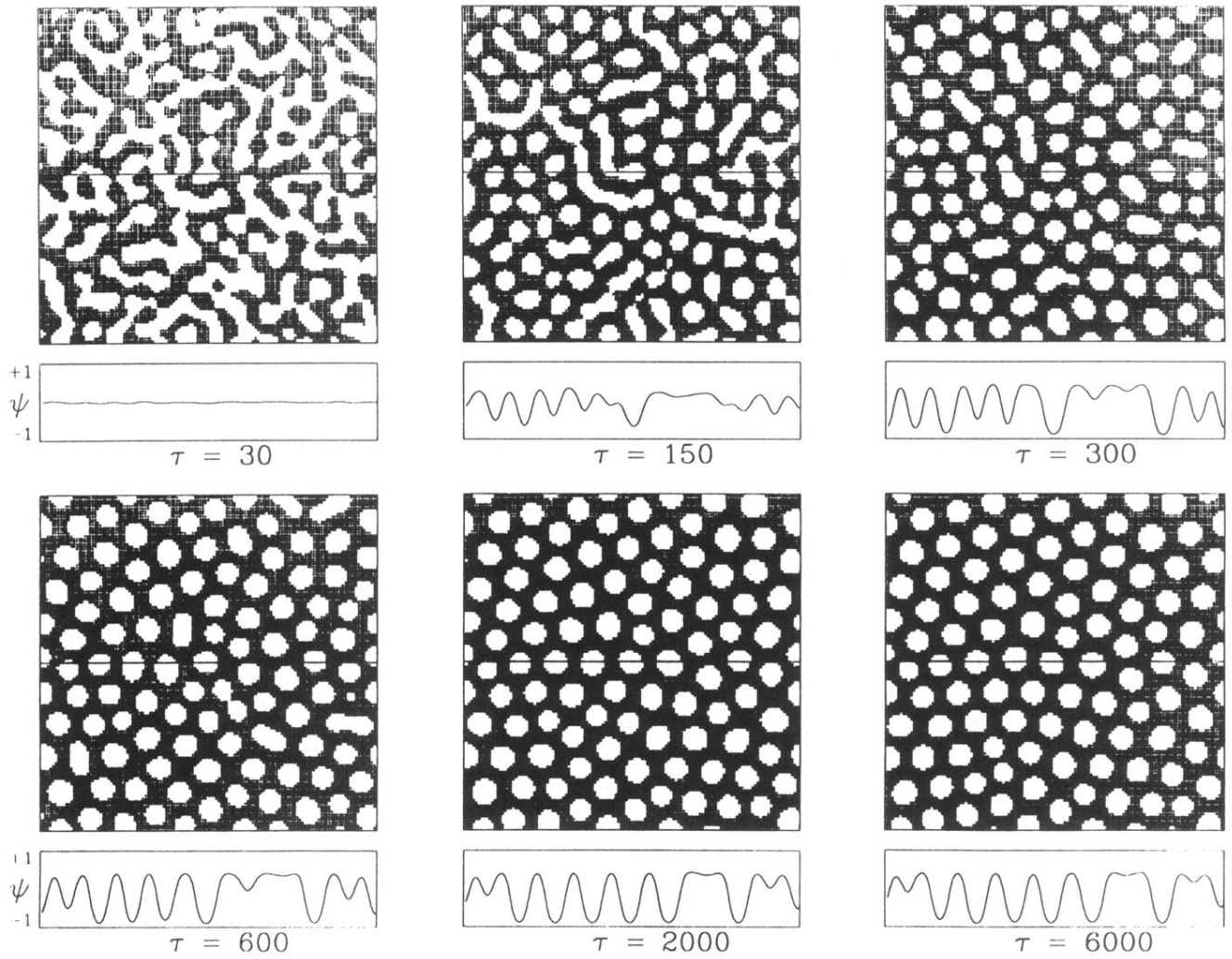


FIG. 12. Configuration pictures corresponding to  $MB_L$  for an off-critical quench in the thick film. (Run *C*:  $L = 10$ ,  $\beta = 0.22$ , and  $\psi_0 = 0.2$ .)

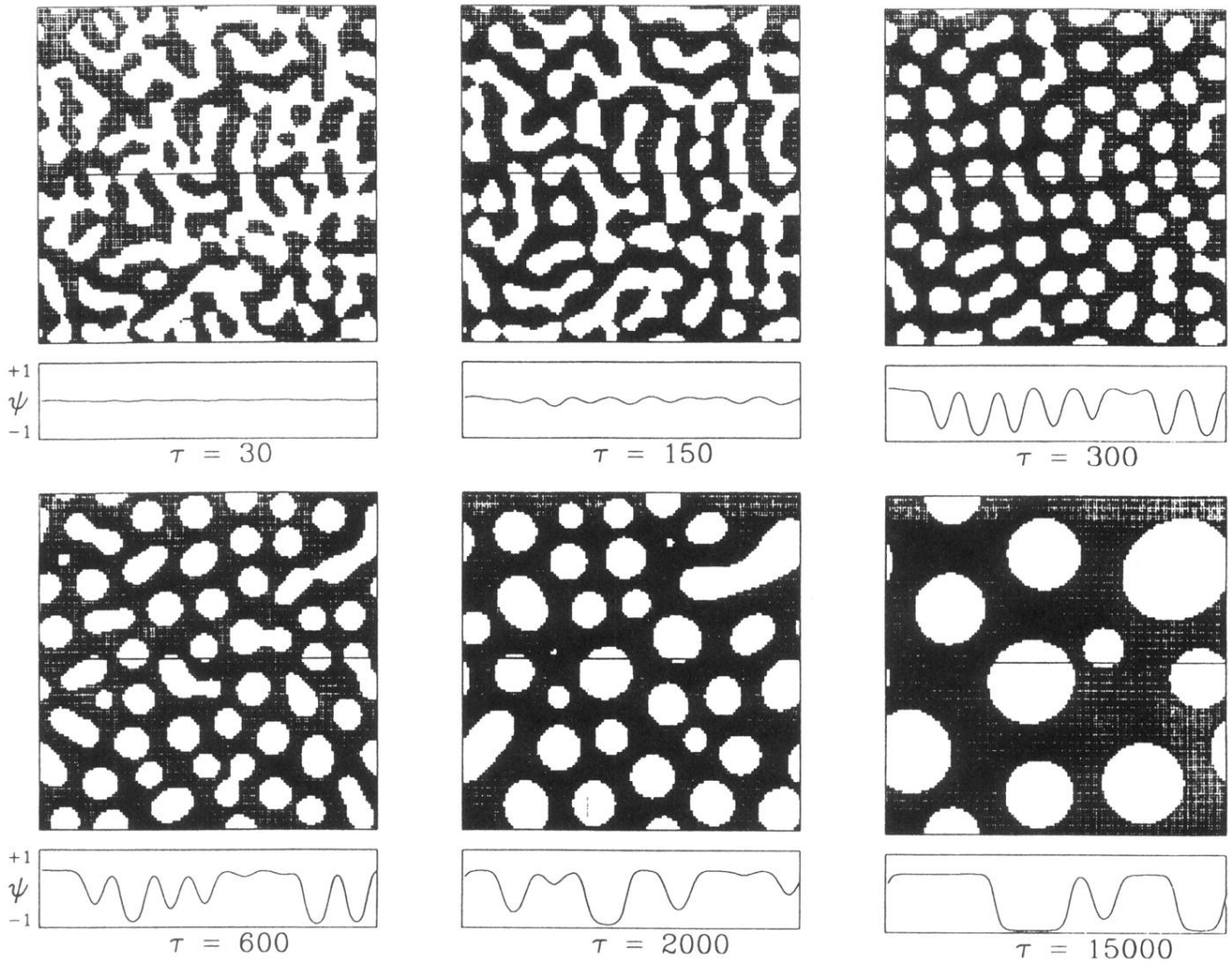


FIG. 13. Configuration pictures corresponding to  $MB_L$  for an off-critical quench in the thin film. (Run  $D$ :  $L = 0.1$ ,  $\beta = 5$ , and  $\psi_0 = 0.2$ .)

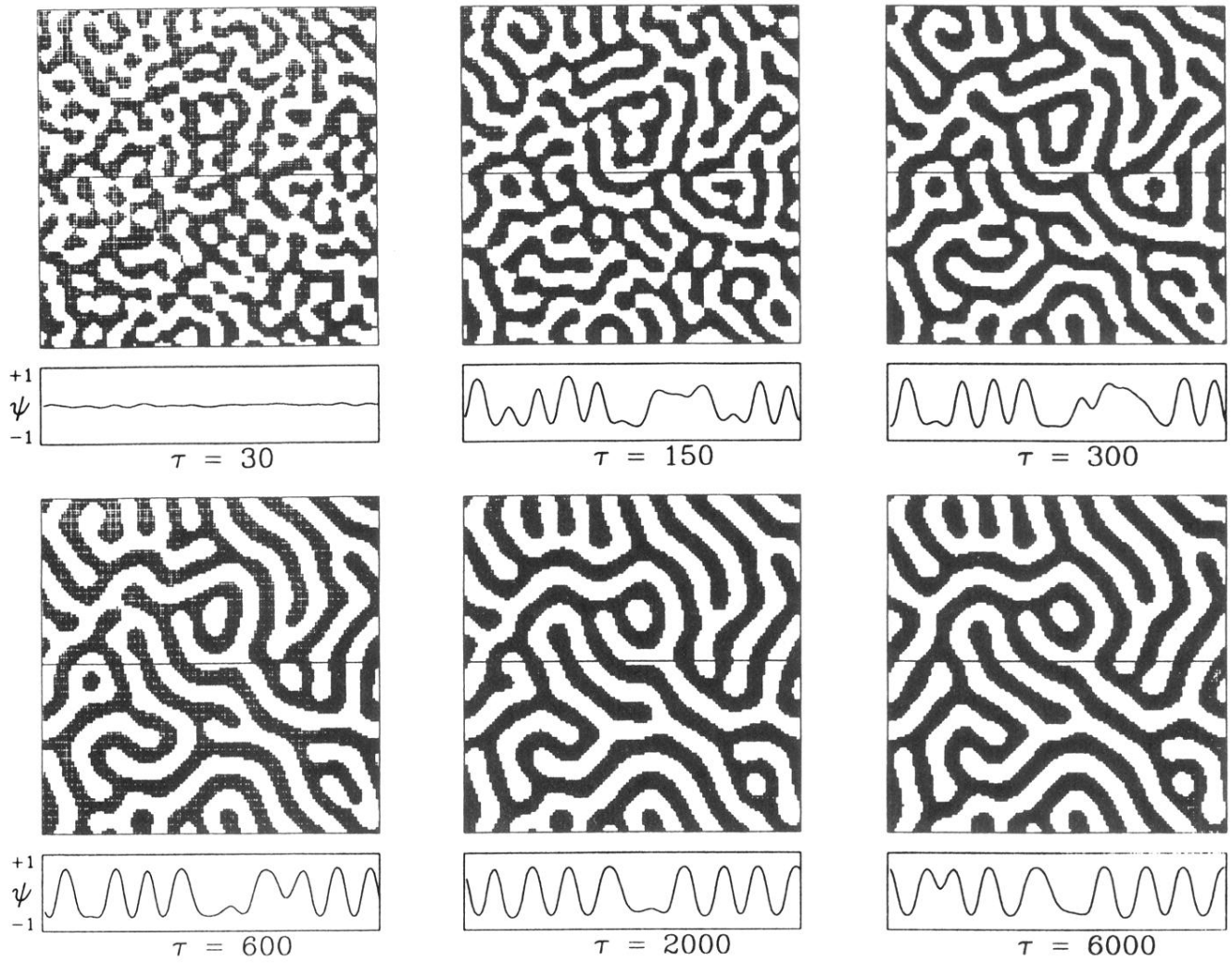


FIG. 5. Configuration pictures corresponding to  $MB_L$  for a critical quench in the thick film. (Run A:  $L = 10$ ,  $\beta = 0.22$ , and  $\psi_0 = 0$ .)

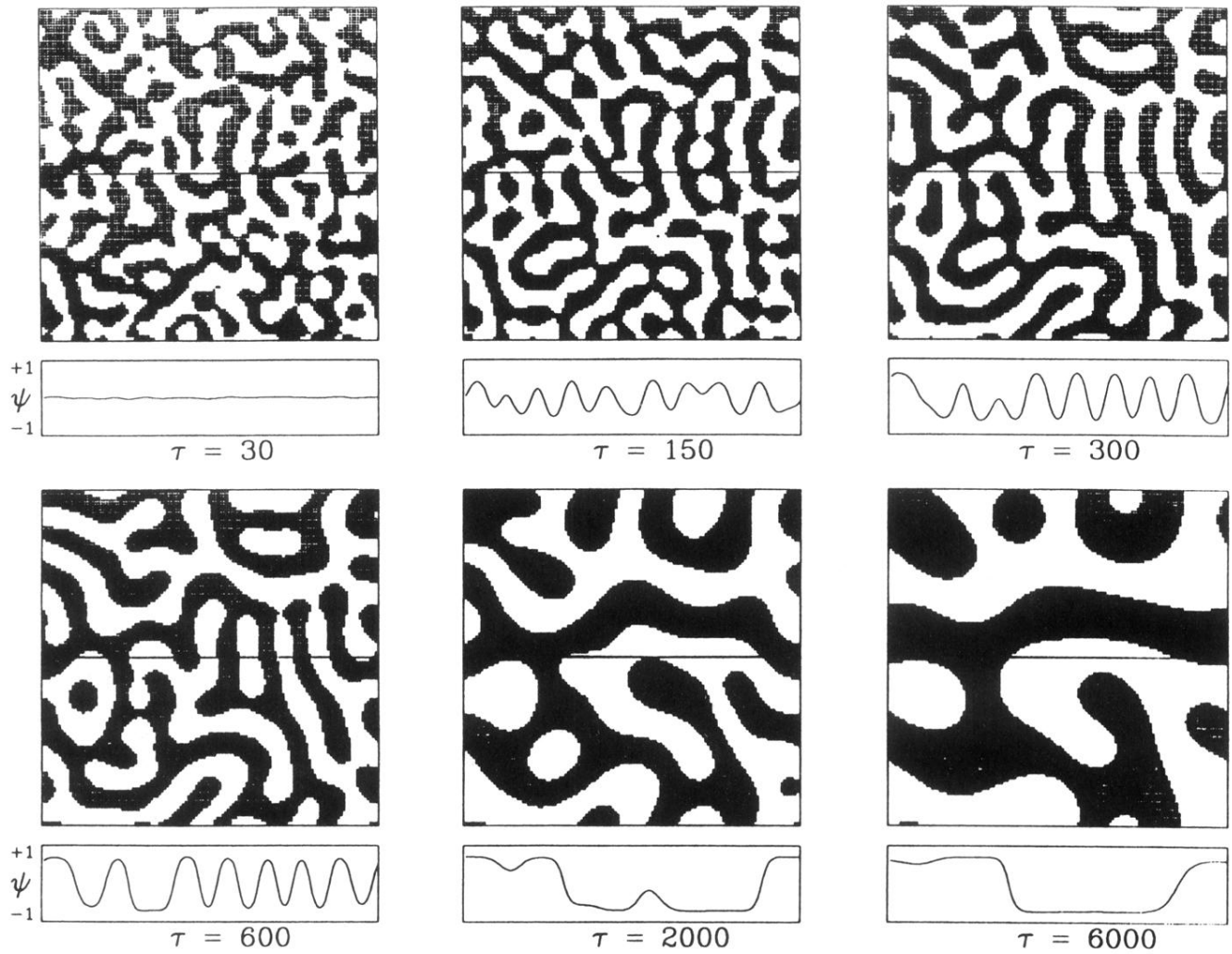


FIG. 6. Configuration pictures corresponding to  $MB_L$  for a critical quench in the thin film. (Run *B*:  $L = 0.1$ ,  $\beta = 5$ , and  $\psi_0 = 0$ .)